Article

Cell

Systemic Immunity Is Required for Effective Cancer Immunotherapy

Graphical Abstract

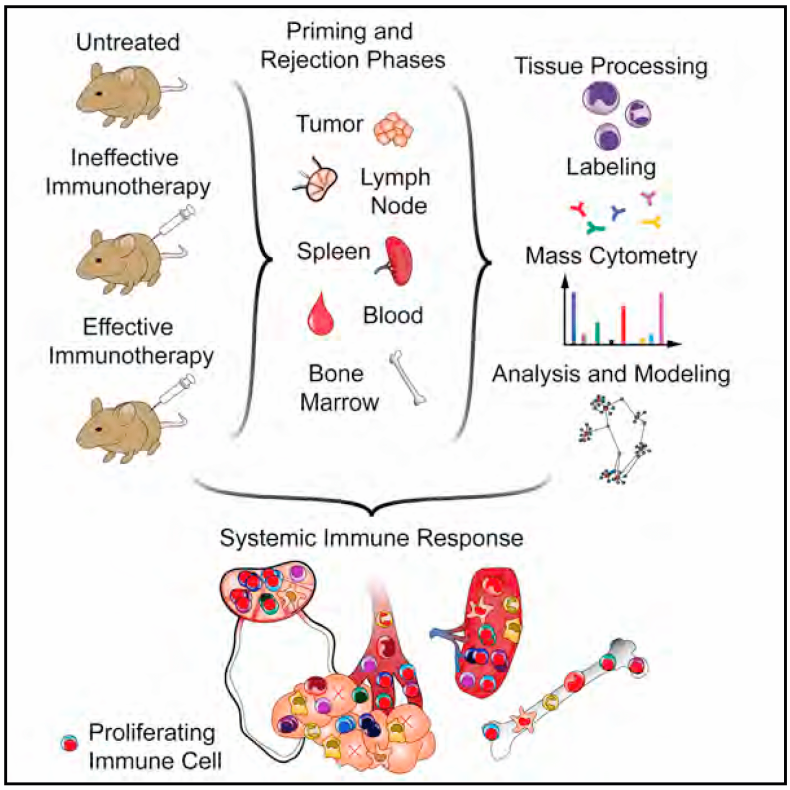

Authors

Matthew H. Spitzer, Yaron Carmi, Nathan E. Reticker-Flynn, ..., Lawrence Fong, Garry P. Nolan, Edgar G. Engleman

Correspondence

matthew.spitzer@ucsf.edu (M.H.S.), gnolan@stanford.edu (G.P.N.), edengleman@stanford.edu (E.G.E.)

In Brief

A systems approach reveals that engagement of systemic immunity is critical to the process of tumor rejection following immunotherapy.

Highlights

- System-wide models reveal coordinated anti-tumor immunity across the organism
- Tumor eradication requires immune activation in the periphery
- Network analysis identifies CD4 T cells sufficient to initiate immune responses
- PD-L1 upregulation early post-therapy protects distal tumors from systemic immunity

Spitzer et al., 2017, Cell *168*, 1–16
January 26, 2017
http://dx.doi.org/10.1016/j.cell.2016.12.022

CellPress

Please cite this article in press as: Spitzer et al., Systemic Immunity Is Required for Effective Cancer Immunotherapy, Cell (2017), http://dx.doi.org/10.1016/j.cell.2016.12.022

Systemic Immunity Is Required for Effective Cancer Immunotherapy

Matthew H. Spitzer,[1,2,3,4,6,8,9,*] Yaron Carmi,[1,7,8] Nathan E. Reticker-Flynn,[1,8] Serena S. Kwek,[5] Deepthi Madhireddy,[2] Maria M. Martins,[1] Pier Federico Gherardini,[2] Tyler R. Prestwood,[1] Jonathan Chabon,[1] Sean C. Bendall,[1] Lawrence Fong,[5,6] Garry P. Nolan,[2,3,*] and Edgar G. Engleman[1,3,*]

[1]Department of Pathology
[2]Baxter Lab in Stem Cell Biology, Department of Microbiology and Immunology
[3]Program in Immunology
Stanford University, Stanford, CA 94305, USA
[4]Department of Microbiology and Immunology
[5]Division of Hematology and Oncology, Department of Medicine
[6]Helen Diller Comprehensive Cancer Center
University of California, San Francisco, San Francisco, CA 94143, USA
[7]Department of Pathology, The Sackler School of Medicine, Tel-Aviv University, Ramat Aviv 69978, Israel
[8]Co-first author
[9]Lead Contact
*Correspondence: matthew.spitzer@ucsf.edu (M.H.S.), gnolan@stanford.edu (G.P.N.), edengleman@stanford.edu (E.G.E.)
http://dx.doi.org/10.1016/j.cell.2016.12.022

SUMMARY

Immune responses involve coordination across cell types and tissues. However, studies in cancer immunotherapy have focused heavily on local immune responses in the tumor microenvironment. To investigate immune activity more broadly, we performed an organism-wide study in genetically engineered cancer models using mass cytometry. We analyzed immune responses in several tissues after immunotherapy by developing intuitive models for visualizing single-cell data with statistical inference. Immune activation was evident in the tumor and systemically shortly after effective therapy was administered. However, during tumor rejection, only peripheral immune cells sustained their proliferation. This systemic response was coordinated across tissues and required for tumor eradication in several immunotherapy models. An emergent population of peripheral CD4 T cells conferred protection against new tumors and was significantly expanded in patients responding to immunotherapy. These studies demonstrate the critical impact of systemic immune responses that drive tumor rejection.

INTRODUCTION

Since the use of bacterial vaccines for the treatment of cancer over a century ago (Coley, 1893), evidence demonstrating the ability of the immune system to reject tumors has mounted. Several immunotherapeutic strategies have now yielded sustained clinical responses, including blocking antibodies against suppressive receptors (Topalian et al., 2015) and transfer of adoptive T cells (Restifo et al., 2012), dendritic cells (Kantoff et al., 2010), or engineered T cells (Porter et al., 2011). For specific immunotherapies, individual cell subsets have been examined for mechanistic roles, and features have been correlated with responsiveness (Herbst et al., 2014). However, a comprehensive understanding of the global immune dynamics that mediate effective anti-tumor immunity remains unclear. Because most cancer patients do not respond to immunotherapy, there is an urgent need to improve upon the current toolkit, especially for adenocarcinomas, the most common forms of cancer.

Another gap in our knowledge is which anatomic sites drive anti-tumor immunity. Expansion of tumor-infiltrating T cells has shown striking results in melanoma, demonstrating that effective cells can be found within the microenvironment (Restifo et al., 2012). In contrast, dendritic cell vaccines can stimulate de novo T cell responses and have shown efficacy (Kantoff et al., 2010). For strategies that initiate anti-tumor immunity in the patient, it remains unclear where immune cell activation takes place. For example, in the case of CTLA-4 blockade, administering antibody into the tumor can induce rejection (Simpson et al., 2013) and is dependent on Fcγ receptors (Bulliard et al., 2013), consistent with depleting intratumoral regulatory T cells and releasing local effector cells. However, new tumor-reactive T cell clones emerge in patients experiencing clinical benefit, suggestive of new priming (Kvistborg et al., 2014). For other strategies to induce immune responses in situ, this question has not been addressed conclusively.

New methods of assessing the immune state under any given condition allow us to systematically address this question by characterizing diverse cell subsets and their activation states simultaneously. Mass cytometry builds upon the success of flow cytometry and enables over 40 simultaneous parameters to be quantified by replacing fluorophores with mass tags (Bandura et al., 2009; Bendall et al., 2011). It is thus possible to discern the identity and behavior of numerous cell types from a single experiment (Bendall et al., 2011; Spitzer et al., 2015). Using a spontaneous model of triple-negative breast cancer, we

assessed immune cell dynamics across the organism during tumor rejection.

RESULTS

Tumor-Binding Antibodies Combined with Dendritic Cell Adjuvants Induce Potent T Cell Immunity against Spontaneous Breast Tumors

To characterize effective anti-tumor immunity, we chose a therapy with efficacy in multiple cancer types. We recently described the combination of tumor-binding antibodies and adjuvants to stimulate dendritic cells as a means of inducing potent T cell-mediated immunity (Carmi et al., 2015). Beyond melanomas, this strategy was effective against Lewis lung and 4T1 breast carcinomas. While carcinomas are the most common class of cancer, more limited progress has been made in immunotherapy against these compared to melanoma or hematological malignancies (Topalian et al., 2015). Therefore, we determined whether this approach would be effective in a widely used spontaneous model of carcinoma, MMTV-PyMT (murine mammary tumor virus-polyoma middle T) triple-negative breast cancer, which is refractory to other immunotherapies such as checkpoint blockade (i.e., anti-programmed death-1 [anti-PD-1]) (Bos et al., 2013).

Once animals developed a tumor of 25 mm^2, they were injected intratumorally with allogeneic tumor-binding immunoglobulin G (IgG) (alloIgG) antibodies combined with anti-CD40 antibody and interferon γ (IFNγ) (Carmi et al., 2015). Treated animals experienced regression of the injected lesion (Figure 1A). We previously established that the efficacy of this therapy in melanoma depends on T cell responses. Treated MMTV-PyMT tumors were infiltrated by CD8 T cells, concurrent with tumor shrinkage and tumor cell death indicated by TUNEL staining (Figures 1B and 1C).

We devised an experimental strategy for elucidating the system-wide immunological underpinnings of this response (Figure 1D). AlloIgG from CD-1 and C57BL/6 mice bound MMTV-PyMT breast tumor cells (Figure 1E). Mice were randomized to one of those sources of alloIgG, ensuring that responses were not specific to one antibody source. Anti-PD-1 served as a model of ineffective therapy due to its wide clinical use but lack of efficacy in this model. PyMT-expressing females were randomized to treatment groups as follows: B6-alloIgG + anti-CD40 + IFNγ, CD-1-alloIgG + anti-CD40 + IFNγ, anti-PD-1, or no treatment. The mouse began treatment once it developed a tumor of 25 mm^2, which was considered day 0.

We previously determined that immune activation is discernable by 3 days after treatment (i.e., "priming phase"), with tumor shrinkage by day 8 (i.e., "rejection phase"). At these time points, we sacrificed mice from each treatment (n = 3–4 per treatment, per time point) and prepared tissues for mass cytometry. Animals receiving therapy with alloIgG experienced significant tumor regression by day 8, with no significant difference between untreated animals and those receiving anti-PD-1 (Figure 1F). This design enabled us to contrast effective and ineffective immune responses.

Immune Cell Proliferation Is Not Maintained in the Tumor Microenvironment during Tumor Rejection

We next sought to systematically define changes in immune cell organization and behavior in the tumor microenvironment between the effective and ineffective treatments. We recently reported a computational method called Scaffold (single-cell analysis by fixed force- and landmark-directed) maps for creating a reference map from high-dimensional single-cell data, facilitating comparisons across samples (Spitzer et al., 2015). These maps provide a data-driven representation of the cells present in a sample while also denoting the location of landmark immune cell populations, defined using prior knowledge of the immune system (Figure S1). These landmarks (visualized as red nodes in the graph in Figure S1) function as flags to orient the investigator. In these graphs, the similarity of two groups of cells is visualized by the length of the edge connecting them. In other words, two groups of cells connected by a short line are similar to one another with respect to the proteins they express (see STAR Methods).

This method was developed in an extensible manner for future datasets to be incorporated, but it did not enable precise statistical comparisons across groups of samples. Another algorithm for mass cytometry analysis, Citrus (Bruggner et al., 2014), provides statistical comparisons between groups. The results from Citrus, however, can be cumbersome to interpret. We therefore determined whether the statistical inference integrated into Citrus could, instead, be applied to Scaffold maps. We call this hybrid method "Statistical Scaffold" (Figure S1). We altered the first step of Scaffold maps, clustering data from all tumor specimens together to define cell groups in an unbiased manner. This enables direct comparisons across samples. We then used the Significance Analysis of Microarrays framework to identify statistically significant features between the sample types (effective versus ineffective treatment groups) as in Citrus (Bair and Tibshirani, 2004; Bruggner et al., 2014). The resulting Scaffold maps can then be colored by statistical significance, where features with q values less than 0.05 (adjusted for multiple testing) are given either in red or in blue, depending on the directionality of the change (e.g., up or down in the group that received effective therapy). These features can be changes in either the frequency or the molecular expression of a particular cell subset.

Because the text identifying landmark populations can be obscured, an empty reference graph can be found in Figure S2. The frequency, coefficient of variation, and protein expression of each cluster are shown in Figure S3 and Table S2. Because the plasmacytoid dendritic cells (pDCs) are far from other cell populations in the graph, they are displayed in an inset image (Figures 2, 3, and 4, black dashed outline).

We began applying Statistical Scaffold to data from the tumor specimens collected during the priming phase. In animals treated with effective therapies, a large number of immune cells increased in frequency as a percentage of total cells in the tumor, consistent with an anti-tumor immune response (Figure 2A). Very few differences existed between untreated mice and those receiving the ineffective anti-PD-1 therapy (Figures S2B–S2E), demonstrating that effective therapy initiated a fundamentally different immune response. We therefore asked how these cell populations were changing with effective therapy at the molecular level, leveraging the interactivity of Scaffold maps to visualize protein expression between the treatment groups.

Subsets of macrophages increasing in frequency with effective treatment expressed high levels of the immunosuppressive

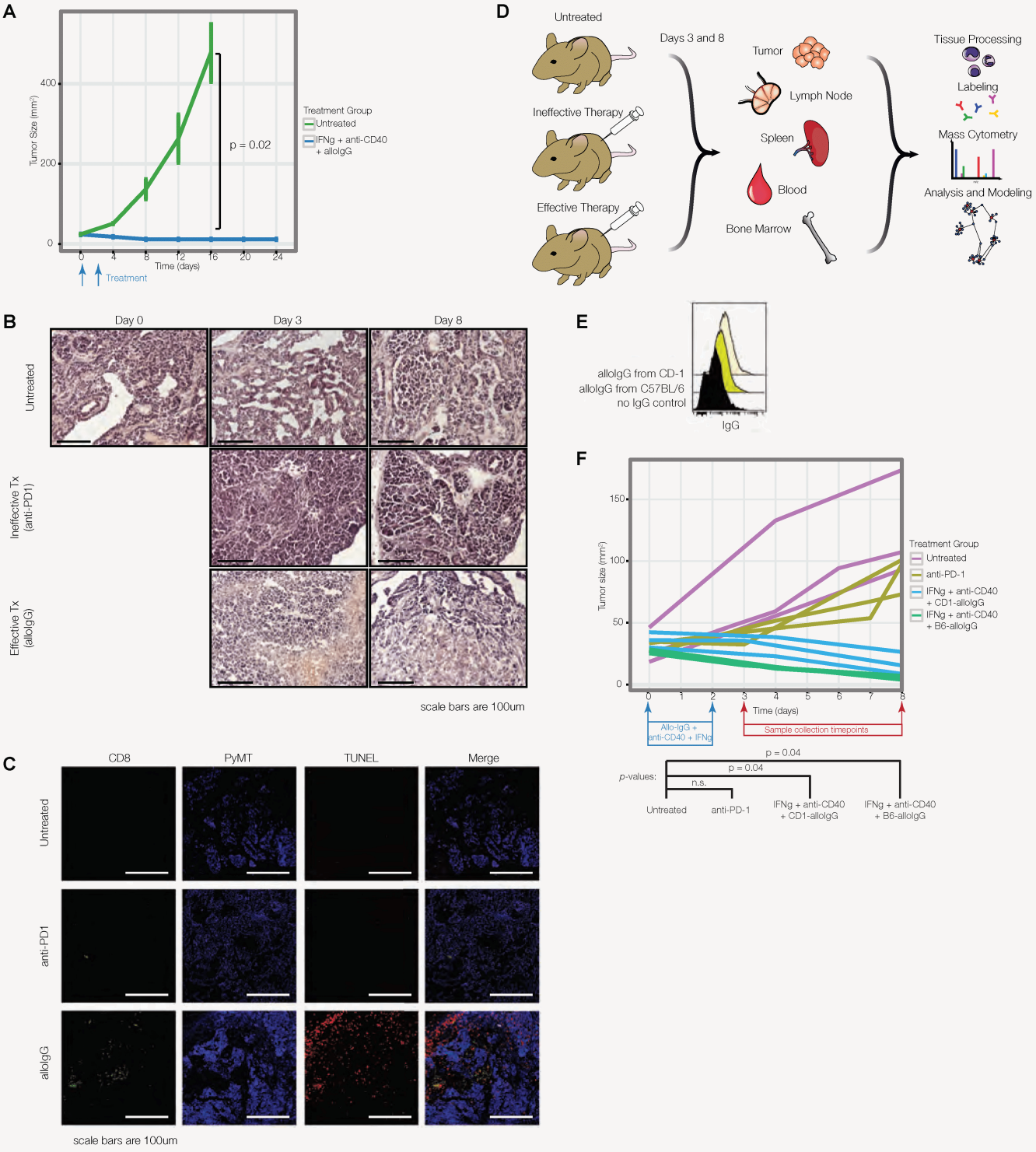

Figure 1. Tumor-Binding Antibodies and Dendritic Cell Adjuvants Induce Rejection of Spontaneous Breast Tumors

(A) MMTV-PyMT mice with tumors of 25 mm^2 treated with allogeneic IgG pooled from C57BL/6 and CD-1 mice, treated with anti-CD40 and IFNγ, or untreated.

(B and C) H&E (B) and immunofluorescence (C) of tumors from treated mice 8 days after therapy.

(D) Mass cytometry experiment.

(E) Binding of IgG antibodies from naive CD-1 or C57BL/6 mice to MMTV-PyMT tumor cells.

(F) Tumor sizes, at day 8 after therapy, for mass cytometry.

See also Figure S1 and Table S1.

Please cite this article in press as: Spitzer et al., Systemic Immunity Is Required for Effective Cancer Immunotherapy, Cell (2017), http://dx.doi.org/10.1016/j.cell.2016.12.022

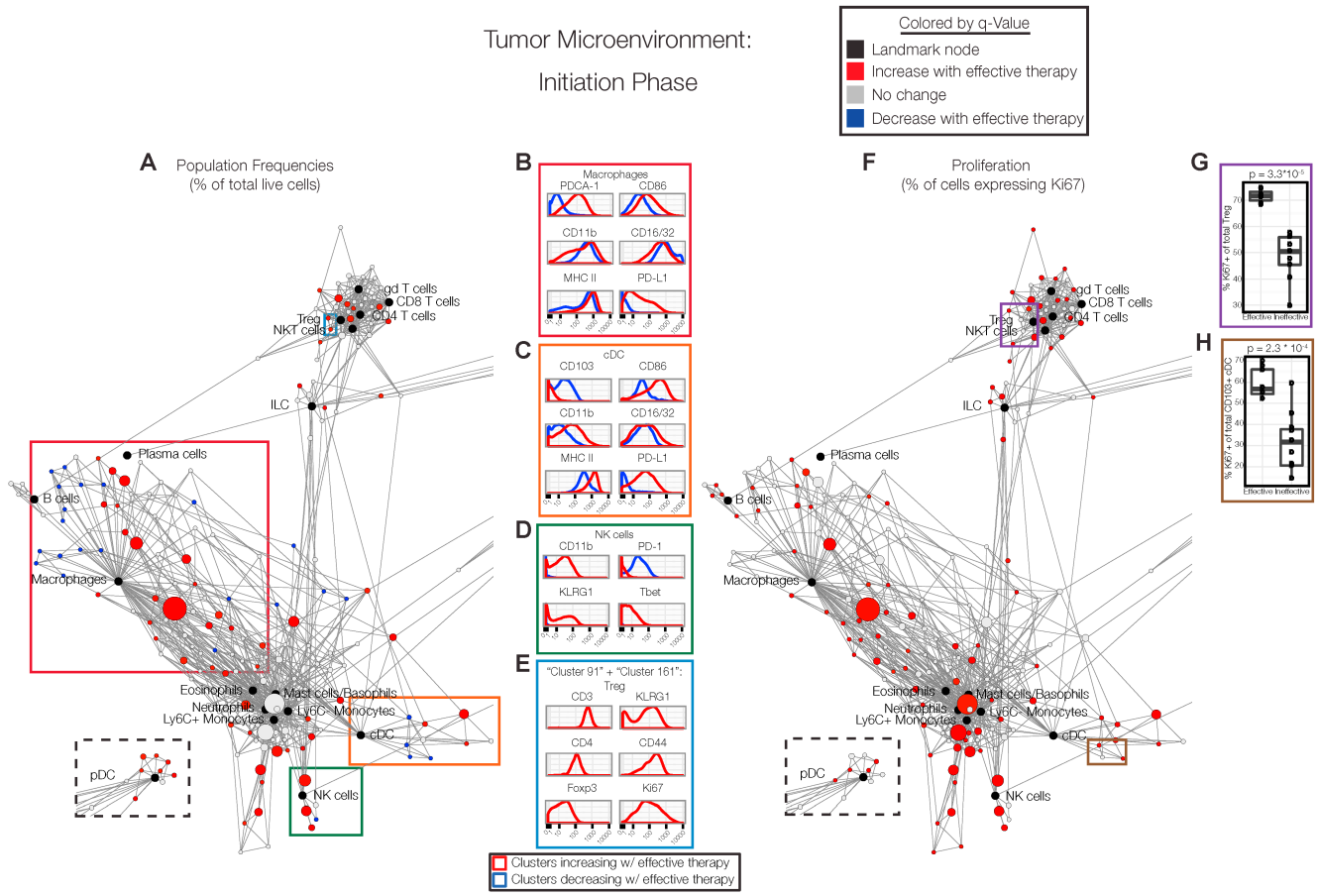

(legend on next page)

Please cite this article in press as: Spitzer et al., Systemic Immunity Is Required for Effective Cancer Immunotherapy, Cell (2017), http://dx.doi.org/10.1016/j.cell.2016.12.022

co-receptor programmed death-ligand 1 (PD-L1) and plasmacytoid dendritic cell antigen 1 (PDCA-1), both of which are inducible by IFNγ. Additionally, these cells had high expression of the co-stimulatory receptor CD86 and major histocompatibility complex class II (MHC class II), indicating activation and enhanced antigen presentation. A small decrease in the expression of Fcγ receptors (FcγRs) CD16/32 could reflect internalization upon ligation by alloIgG (Figure 2B).

Classical dendritic cells (cDCs) increasing during the priming phase also expressed high levels of CD86, MHC class II and PD-L1 (Figure 2C). The integrin CD103 mediates trafficking to the tissues and is expressed by cross-presenting DC that can promote anti-tumor immunity (Broz et al., 2014). Interestingly, this population significantly decreased in tumors after effective therapy, perhaps indicating migration. Dendritic cells (DCs) increasing in frequency after effective therapy displayed higher variance in FcγR CD16/32 expression, consistent with modulation of this pathway during effective therapy with alloIgG. Concurrently, there was also an unexpected increase in myeloid populations traditionally thought to be immunosuppressive in cancer, such as $Ly6C^+$ monocytes and $Ly6G^+$ neutrophils (Gabrilovich et al., 2012).

Natural killer (NK) cell subsets markedly increased with higher expression of CD11b, killer-cell lectin-like receptor G1 (KLRG1), and the transcription factor T-bet, consistent with an effector phenotype (Figure 2D). These cells had little expression of the immunosuppressive co-receptor PD-1.

Several types of T cells expanded significantly with effective therapy. Several increasing subsets were attributable to conventional CD4 and CD8 T cells. Contrary to expectations, however, regulatory T cells (Tregs) expressing the transcription factor Foxp3 were also more prevalent after effective therapy (Figure 2E). These cells co-expressed KLRG1 and CD44, denoting an increase in effector Tregs (Cheng et al., 2012) present in the tumor. The frequency of Tregs has been suggested as a negative prognostic feature for various tumors (Bates et al., 2006; Curiel et al., 2004). Based on our data, utilizing this metric would be quite misleading. Taken together, these results demonstrate the complex dynamics that underlie productive anti-tumor immunity, including the effector and regulatory arms of myeloid and lymphoid lineages.

We next queried whether changes in immune cell proliferation within the tumor were observed. During the priming phase, a large portion of immune cell types exhibited increased rates of proliferation with effective therapies, evident by the proportion of cells expressing Ki67 (Figure 2F), including Tregs (Figure 2G). Despite decreasing in frequency, CD103+ DCs also exhibited higher proliferation (Figure 2H), suggesting that these cells do become activated. Thus, the priming phase of the effective anti-tumor immune response is characterized by broad expansion of leukocytes as well as enhanced proliferation in the tumor microenvironment across many immune cell types.

We next mapped the dynamics of intratumoral immune cells during the rejection phase (8 days after therapy) (Figure 2I). Similar changes to those seen in the priming phase were observed in the macrophage compartment during tumor rejection, consistent with activation (Figure 2J). The frequency of B cell subsets and innate lymphoid cells (ILCs) also increased during the rejection phase. One prominent ILC cluster (outlined in orange) contained cells expressing FcγRs, some of which expressed T-bet (Figure 2K). Manual identification of T-bet+ type-1 ILCs confirmed their increased prevalence (Figure 2L). Numerous clusters of T cells were also significantly expanded with effective therapy, including effector memory CD4 and CD8 T cells (Figures 2M and 2N) as well as Tregs.

In stark contrast to the priming phase, there was no difference in the rate of proliferation across immune cells in the tumor microenvironment during the rejection phase (Figure 2O). Similar results were found in a genetically engineered inducible mouse model of melanoma driven by $Braf^{V600E}$ and loss of *Pten* (referred to as BP melanoma mice) on day 8 after treatment with effective therapy (Figure S3A) (Dankort et al., 2009). We therefore hypothesized that other anatomical locations were responsible for sustaining the immune response during the rejection phase.

Lymphocyte Activation and Proliferation Are Maintained in the Secondary Lymphoid Organs throughout the Immune Response

We next analyzed the immune cell composition in the tumor-draining lymph nodes of treated animals. During the priming phase, several specific clusters of lymphocytes expanded in frequency (Figure 3A). Marked expansion of activated, naive B cells expressing immunoglobulin M (IgM) and high levels of CD44, CD86, and MHC class II, but low levels of immunoglobulin D (IgD), was observed (Figure 3B).

In the T cell compartment, a cluster of Th1 cells (CD44+T-bet+) emerged with effective therapy with a unique phenotype

Figure 2. The Tumor Microenvironment Is Remodeled and Immune Cells Transiently Proliferate during Effective Responses

(A) Statistical Scaffold map of the tumor on day 3. Black nodes are landmark nodes, representing canonical cell populations identified manually. Other nodes reflect unsupervised clustering of live leukocytes (see STAR Methods). Clusters in red denote populations significantly higher in frequency with effective therapy; blue clusters are significantly lower in frequency. pDCs are in the dashed box to maximize space. Colored boxes are populations analyzed in (B)–(E).

(B–E) Expression profile of (B) B cell, (C) cDC, (D) NK cell, or (E) Treg cell clusters expanding with effective therapy (red) versus those decreasing (blue).

(F) Scaffold map of Ki67 expression in immune cells in the tumor on day 3. Subsets more proliferative after effective therapy are indicated in red.

(G) Percentage of Ki67+ Tregs.

(H) Percentage of Ki67+ cDCs.

(I) Scaffold map of the tumor on day 8.

(J) Expression profile of macrophage clusters expanding with effective therapy (red) versus those decreasing (blue).

(K) Expression profile of ILC cluster increasing with effective therapy.

(L) ILC1 frequencies.

(M and N) Expression profile of (M) CD4 T cell cluster or (N) CD8 T cell cluster increasing with effective therapy.

(O) Scaffold map of Ki67 expression in immune cells in the tumor on day 8.

See also Figures S2, S3, and S4 and Tables S2 and S3.

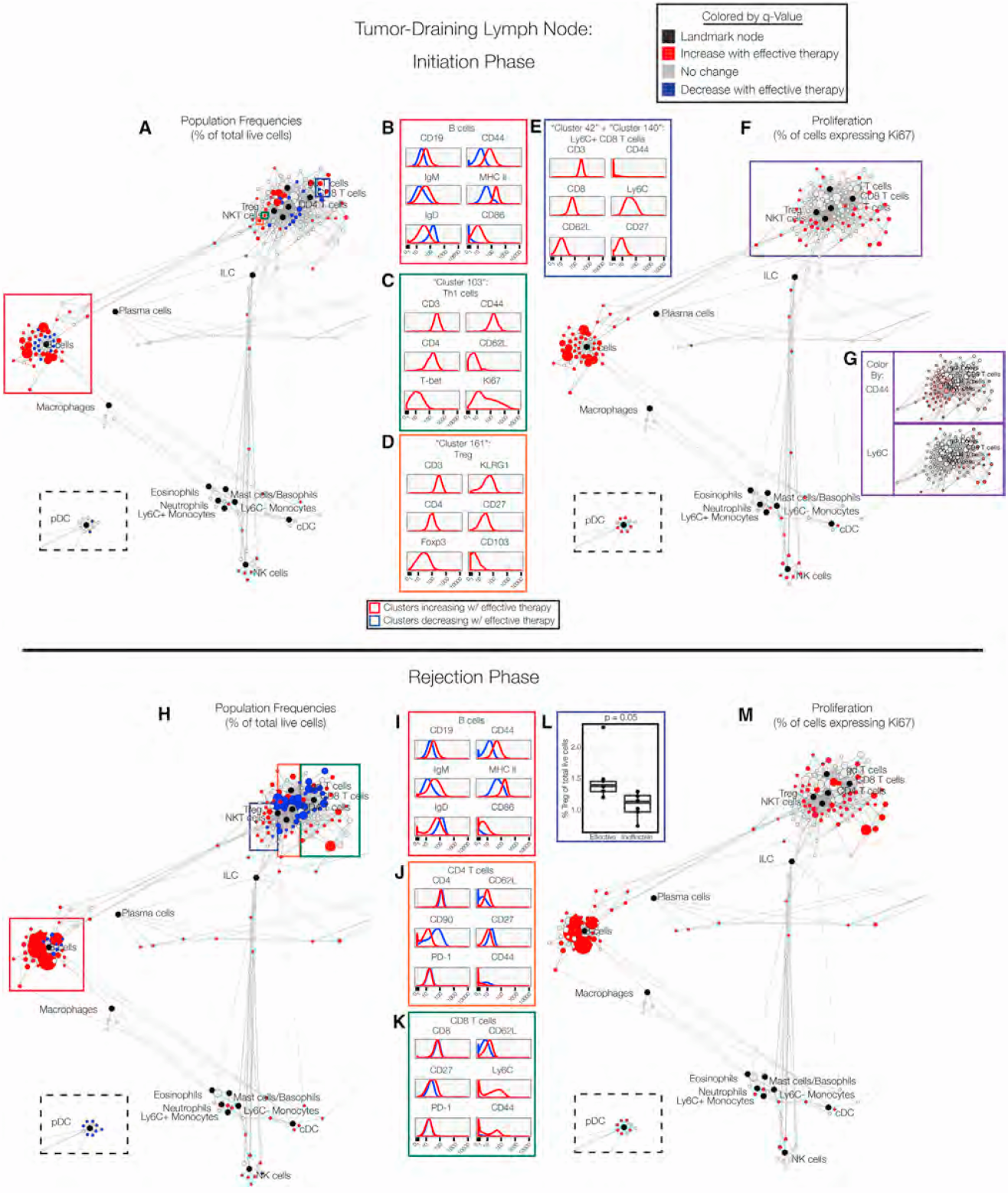

Figure 3. Cells in the Tumor-Draining Lymph Node Display Sustained Activation

(A) Scaffold map of the draining lymph node on day 3.

(B) Expression profile of B cell clusters expanding with effective therapy (red) versus those not changing (black).

(C–E) Expression profile of (C) Th1, (D) Treg, or (E) CD8 T cell clusters increasing with effective therapy.

(legend continued on next page)

Please cite this article in press as: Spitzer et al., Systemic Immunity Is Required for Effective Cancer Immunotherapy, Cell (2017), http://dx.doi.org/10.1016/j.cell.2016.12.022

(CD90^{hi}CD69+CD62L−CD27−KLRG1−) and active proliferation (Ki-67+) (Figure 3C). Additionally, a Treg subset with a similar molecular profile to intratumoral Tregs (KLRG1^{hi}CD103+) significantly expanded (Figure 3D). The CD8 T cells that became more prevalent with effective therapy had some features of central memory cells (Ly6C+ and CD62L+), though they did not upregulate CD44 expression (Figure 3E) (Hänninen et al., 2011; Wherry et al., 2007).

Analysis of proliferation in the draining lymph node revealed active cell division across many cell types during the priming phase of an effective anti-tumor immune response (Figure 3F). Nearly all clusters of B cells, NK cells, cDCs, pDCs, and ILCs displayed enhanced Ki67 expression. Effector/memory T cell clusters (CD44+ or Ly6C+) exhibited significant increases in proliferation (Figure 3G), consistent with the development of a T cell-mediated immune response.

The rejection phase in the tumor-draining lymph node displayed similarly complex dynamics (Figure 3H). Similar changes in the B cell compartment were observed as during the initiation phase (Figure 3I), which may, in part, be in response to anti-CD40. Both increasing CD4 and CD8 T cell subsets exhibited higher expression of CD62L without a change in PD-1 levels (Figures 3J and 3K). A subset of expanding CD8 T cells also expressed Ly6C and CD44 (Figure 3K), denoting the formation of central memory CD8 T cells. Consistent with the tumor microenvironment, Tregs also increased in frequency (Figure 3L), once again highlighting immune regulation.

In contrast to the tumor microenvironment, however, significant increases in leukocyte proliferation across the system were observed during the rejection phase in the draining lymph node (Figure 3M). This observation was also consistent in mice with BP melanoma after therapy (Figure S4B). Furthermore, this trend extended to some naive T cell subsets that had not increased their rates of division during the priming phase (Figure 3M). These dynamics, with elevated proliferation of antigen-experienced cells followed by naive cells, suggest that previously activated T cell clones form a memory immune response, followed by a wave of de novo T cell activation. These results conclusively demonstrate that immune cell proliferation persists in the periphery, even after cells in the tumor microenvironment return to baseline levels of cell division.

We next asked whether the immune response extended into other secondary lymphoid organs such as the spleen, where contact with the treated tumor was less direct. Similar changes were observed in the priming and rejection phases (Figures S5A and S5H), including expansion of activated B cells (Figures S5B and S5I). Plasma cells also increased in frequency, proliferating and upregulating MHC class II, which has been associated with regulation of T cell responses (Figures S5C and S5J) (Pelletier et al., 2010). The T cell and NK cell compartments in the spleen also changed similarly (Figures S5D–S5F and S5K–S5M), including the emergence of a CD90^{hi}Ki-67+ Th1 cell population (Figure S5E). Proliferation in the spleen was also widespread during priming and rejection (Figures S5G and S5N), demonstrating that sustained proliferation is generalizable across secondary lymphoid organs during effective anti-tumor immunity.

Systemic Activation during Effective Immunotherapy Is Captured in Peripheral Blood

To assess whether the responses we observed during tumor rejection were indeed systemic, we analyzed peripheral blood. Profound changes were apparent during the priming phase (Figure 4A). NK cells, cDC, activated B cells, and a subset of activated pDCs (Ly6C+CD4+MHC II^{hi}) all increased in frequency (Figures 4B and 4C). Changes in the T cells paralleled those of the secondary lymphoid organs. CD4 T cell subsets increasing in frequency were largely naive cells (CD62L+CD44−) with no change in PD-1 levels (Figure 4D). The emergence of CD90^{hi} proliferative Th1 cells was also evident (Figure 4E). CD8 T cells increasing in frequency were antigen-experienced cells expressing Ly6C and variable levels of CD44 (Figure 4F). Alterations in circulating monocytes were observed, with subsets of classical (Ly6C^{+}) and non-classical (Ly6C^{-}) monocytes expressing elevated levels of F4/80, the CSF-1 receptor (CD115), MHC class II, and PD-L1, indicative of activation and, perhaps, differentiation to a macrophage-like state (Figures 4G and 4H). Many cell types exhibited increased proliferation as well (Figure 4I), including macrophages, cDCs, pDCs, B cells, NK cells, and many T cell clusters, particularly effector/memory cells. These results support the notion that the priming phase of the anti-tumor immune response is systemic in nature.

The rejection phase in the blood was marked by more substantial decreases in immune cell frequencies (Figure 4J) and an increase in platelet frequencies (Figure 4K). These dynamics may reflect immune cells trafficking into the tissues. Many immune cell populations retained elevated levels of proliferation during the rejection phase (Figure 4L), demonstrative of ongoing immune responses in circulating cells. This was also observed in mice with BP melanoma (Figure S4C). This sustained immune cell proliferation in the blood may present opportunities for non-invasive immune monitoring of anti-tumor immunity.

Immune Remodeling by Effective Immunotherapy Extends to the Bone Marrow

Because the immune response was evidently systemic, we asked whether changes might also take place in the bone marrow, thereby affecting hematopoiesis. Similarly widespread changes were evident (Figures S6A and S6I), involving the emergence of activated B cells, CD4 and CD8 T cells, macrophages, and pDCs (Figures S6B–S6F and S6J–S6N). No changes were

(F) Scaffold map of Ki67 expression in cells in the draining lymph node on day 3.
(G) Expression of CD44 and Ly6C in T cell clusters.
(H) Scaffold map of the draining lymph node on day 8.
(I–K) Expression profile of (I) B cell, (J) CD4 T cell, or (K) CD8 T cell clusters expanding with effective therapy (red) versus those decreasing (blue).
(L) Frequency of Treg clusters.
(M) Scaffold map of Ki67 expression in the draining lymph node on day 8.
See also Figures S4 and S5 and Tables S2 and S3.

Please cite this article in press as: Spitzer et al., Systemic Immunity Is Required for Effective Cancer Immunotherapy, Cell (2017), http://dx.doi.org/10.1016/j.cell.2016.12.022

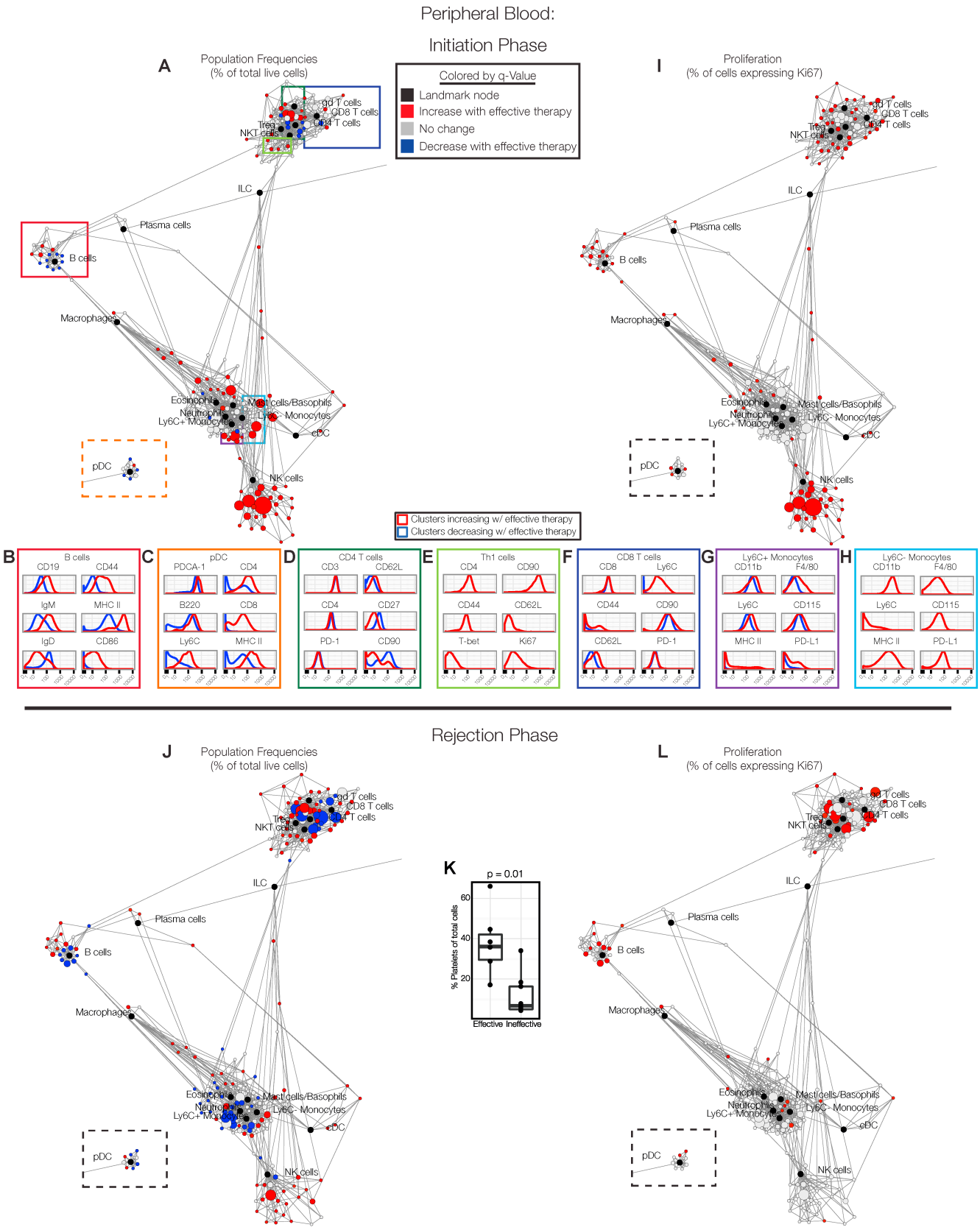

(legend on next page)

observed in the frequency of hematopoietic progenitors (Lineage-cKit+ cells), however (Figures S6G and S6O). Many T cell, B cell, and DC subsets exhibited more proliferation during both the initiation and rejection phases (Figures S6H and S6P), reflecting a truly systemic response.

Systemic Immune Responses Are Required for Tumor Eradication

Effective immunotherapy induces marked changes in both the microenvironment and the periphery, but the prevailing dogma holds that productive immunotherapy functions by reinvigorating immune cells that are actively suppressed in the tumor microenvironment (Jiang et al., 2015). We thus sought to clarify the predominant site in which the anti-tumor immune response was generated. To segregate the immune response in the tumor from the systemic immune response, we treated animals with FTY720, a ligand of the sphinosine-1-phosphate receptor 1, which is required for immune cells to migrate from the secondary lymphoid organs (Matloubian et al., 2004). Treatment was initiated 1 day prior to immunotherapy to inhibit migration caused by immunotherapy. Animals treated with vehicle control and immunotherapy experienced tumor regression, but those co-administered FTY720 had progressive tumor growth (Figure 5A). Therefore, we conclude that the local activation of tumor-infiltrating leukocytes is insufficient to mediate tumor rejection in this system, instead pointing to an essential role for the systemic immune response.

We previously reported that tumor-binding antibody therapy induces tumor-eradicating immune responses in the transplantable 4T1 breast cancer model (Carmi et al., 2015). Consistent with the autochthonous model, blocking leukocyte egress from lymphoid organs prevented regression of 4T1 tumors as well (Figure 5B). Treating these mice again on day 7 after the initial dose resulted in modest tumor shrinkage followed by continued growth, demonstrating that the kinetics of the response were not simply altered by inhibiting leukocyte egress (Figure 5B). Consistently, histological analysis of tumors revealed robust T cell infiltration in animals treated with tumor-binding antibody therapy alone, while simultaneous inhibition of leukocyte egress prevented accumulation of CD4 and CD8 T cells but not CD11b+ myeloid cells (Figure 5C). Inhibition of leukocyte egress also prevented immunological control of metastasis to the lungs (Figures 5D and 5E).

Finally, we assessed whether the T cells in the secondary lymphoid organs were sufficient to induce anti-tumor immunity. After tumor-binding antibody therapy with egress blockade, T cells were transferred from the secondary lymphoid organs into naive animals, which were challenged with 4T1 tumor cells the following day. Consistent with our previous findings, these T cells from the periphery were sufficient to confer protection from 4T1 tumors (Figure 5F). These results rule out the possibility that FTY720 directly prevented the anti-tumor activity of T cells and demonstrate that anti-tumor T cells are induced in the secondary lymphoid organs during the immune response.

Tumor-binding antibody therapy functions by enabling dendritic cell-mediated activation of T cells (Carmi et al., 2015). In contrast, the rejuvenation of exhausted T cells has been suggested as a primary mechanism underlying other immunotherapies, such as checkpoint blockade with anti-PD-1 antibodies (Topalian et al., 2015). We thus determined whether T cell responses in the lymphoid organs were required for productive anti-PD-1 therapy as well. Treatment of mice bearing MC38 colon carcinomas with anti-PD-1 antibodies did induce anti-tumor immune responses capable of controlling tumor growth for up to 2 weeks (Figure 5G). In contrast, tumors in animals treated with anti-PD-1 and FTY720 grew progressively, similarly to untreated animals (Figure 5G). These results demonstrate that a systemic immune response is required for effective immunotherapy across multiple cancer models and therapeutic strategies.

A Peripheral CD4 T Cell Subset Confers Protection to New Tumors

Having established a requirement for peripheral immune responses and previously determined that tumor eradication initiated by tumor-binding antibody therapy is T cell dependent (Carmi et al., 2015), we asked whether we could identify the peripheral T cell subsets that drove tumor eradication. Network analyses have proven effective for identifying dominant elements of a systems-level response (Hotson et al., 2016; Ideker and Krogan, 2012). We therefore calculated immune cell population frequencies from each tissue and calculated pairwise correlations across all animals receiving effective therapy. Indeed, several coordinated modules were readily apparent (Figure 6A). While many immune features in the tumor were concentrated in a single module, features from peripheral tissues were interspersed, demonstrating coordination across organs during the productive immune response. This was especially evident among effector/memory T cell subsets in the peripheral sites (Figure S7A). These modules did not simply represent basal organization at steady state (Figures S7B and S7C), confirming that effective immunotherapy involves new systemic coordination of an immune response.

To identify the key T cell populations that may coordinate the response, we assessed the degree of connectivity of each subset. We generated an adjacency matrix, filtering out weak correlations, and ranked populations by their connectivity in the

Figure 4. Immune Responses Are Sustained in Peripheral Blood

(A) Scaffold map of blood on day 3.

(B–H) Expression profiles of (B) B cell, (C) pDC, (D) CD4 T cell, (E) Th1 cell, (F) CD8 T cell, (G) Ly6C+ monocyte, or (H) Ly6C− monocyte clusters expanding with effective therapy (red histogram) versus those decreasing (blue histogram).

(I) Scaffold map of Ki67 expression in immune cell clusters in blood on day 3.

(J) Scaffold map of blood on day 8.

(K) Frequency of platelets on day 8.

(L) Scaffold map of Ki67 expression in cells in blood on day 8.

See also Figures S4 and S6 and Tables S2 and S3.

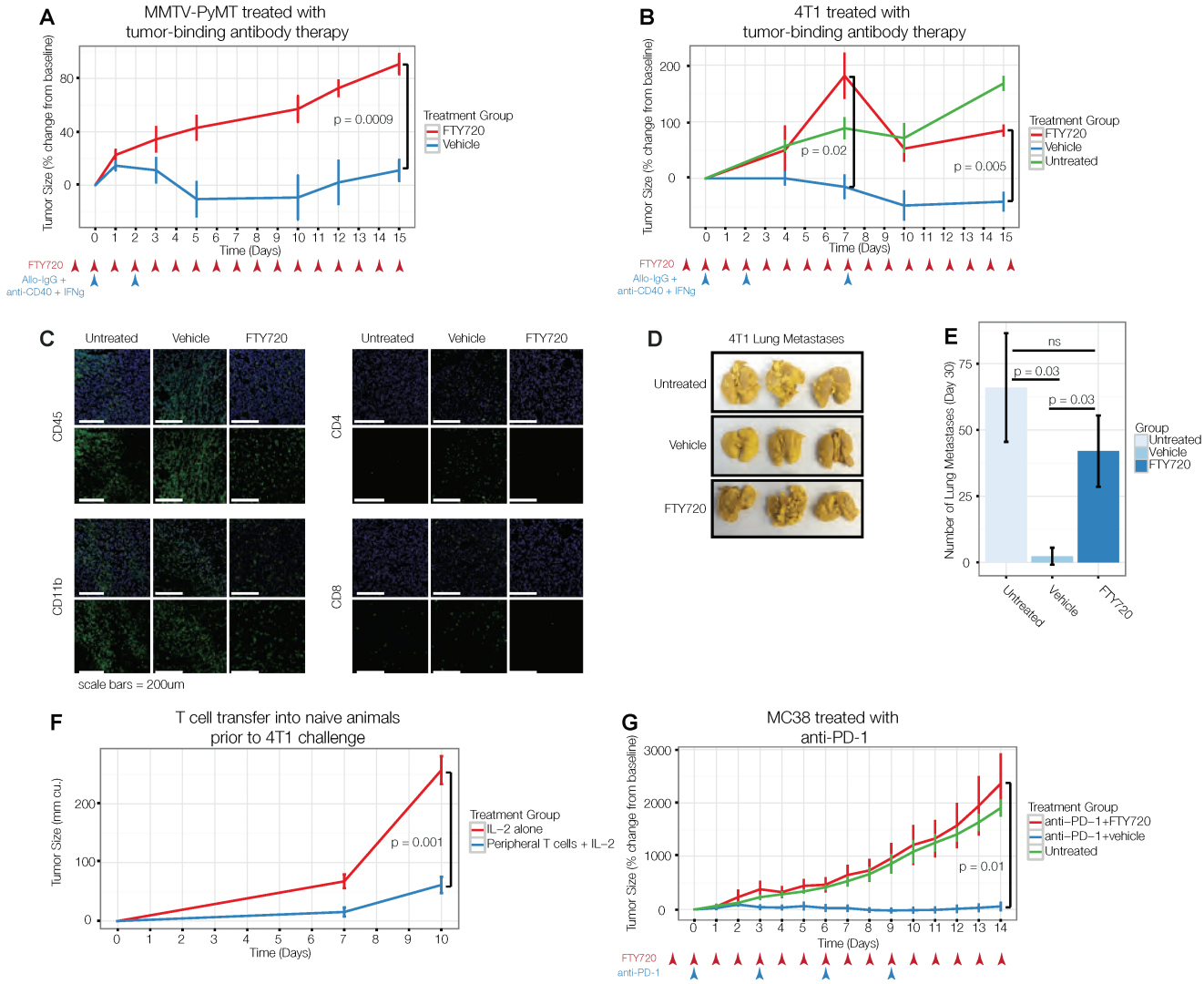

Figure 5. Interfering with Systemic Immune Responses Prevents Effective Immunotherapy

(A) MMTV-PyMT tumor-bearing mice treated with alloIgG, anti-CD40, IFNγ, and daily FTY720 or ethanol control starting 1 day before therapy.

(B) Mice with orthotopic 4T1 tumors treated as in (A).

(C) Immunofluorescence of 4T1 tumors 14 days after therapy.

(D and E) Representative pictures (D) and quantification of 4T1 lung metastases 20 days after therapy (E).

(F) T cells from spleen and lymph nodes of mice with 4T1 tumors, treated with alloIgG, anti-CD40, IFNγ, and FTY720 were transferred with IL-2 into naive BALB/c mice. Controls only received IL-2. Recipients were challenged subcutaneously (s.c.) with 4T1 cells the next day.

(G) MC38 tumor-bearing mice untreated or treated with anti-PD-1 and ethanol control or FTY720.

All p values reflect two-tailed, heteroskedastic t tests in R. Error bars represent SD.

network. Of the T cell subpopulations, seven of the top eight ranking subsets were types of CD4 T cells (Figure 6B). We thus hypothesized that CD4 T cells were more central to the effective immune response than were CD8 T cells, in contrast to the dominant focus on CD8 T cell responses in cancer immunotherapy (Chen and Mellman, 2013; Topalian et al., 2015). Based on the assumption that CD8 T cells are the critical targets for therapy, numerous efforts focus on CD8 CAR T cells or identifying HLA class I epitopes that can be targeted with vaccines.

To address this question experimentally, we treated animals bearing MMTV-PyMT tumors with effective tumor-binding antibody therapy. During tumor rejection, we sacrificed animals, isolated the peripheral lymphoid organs (lymph nodes, spleen, and blood), and sorted antigen-experienced (CD44+) CD4 and CD8 T cells. After expansion in culture, we transferred either the peripheral CD4 or CD8 T cell subsets into untreated animals bearing several large MMTV-PyMT tumors. While both CD4 and CD8 T cells were capable of mediating tumor rejection, animals receiving peripheral CD4 T cells experienced significantly more prolonged protection (Figure 6C).

We then sought to identify the CD4 T cell subset responsible for orchestrating this anti-tumor activity. To investigate whether

Please cite this article in press as: Spitzer et al., Systemic Immunity Is Required for Effective Cancer Immunotherapy, Cell (2017), http://dx.doi.org/10.1016/j.cell.2016.12.022

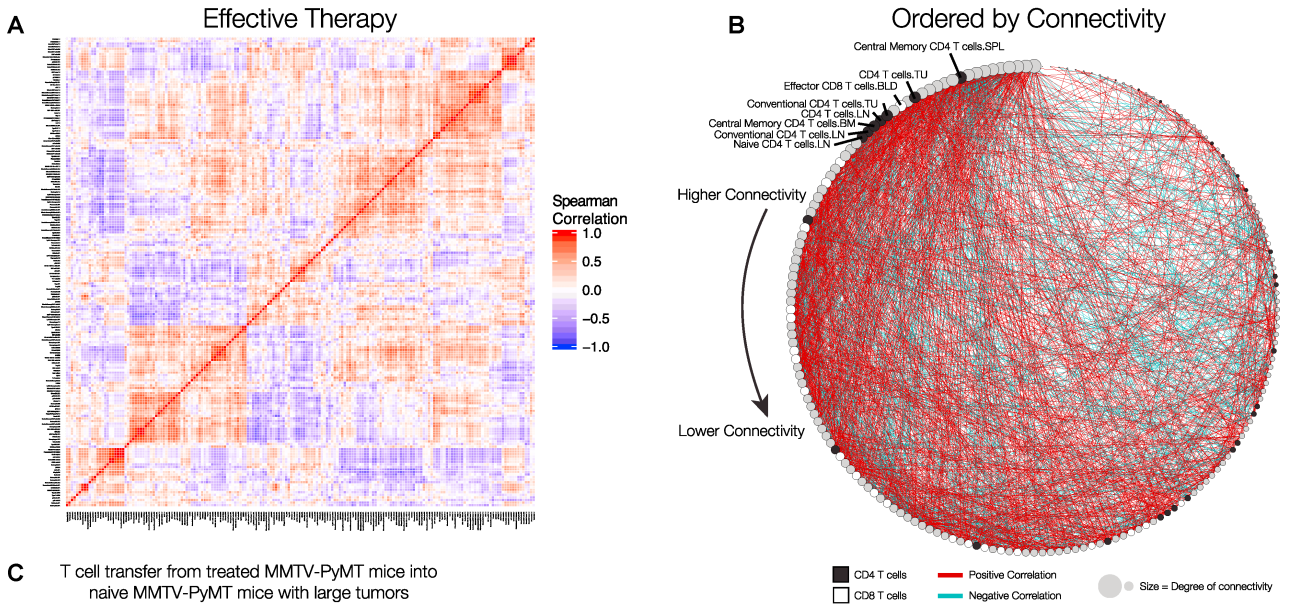

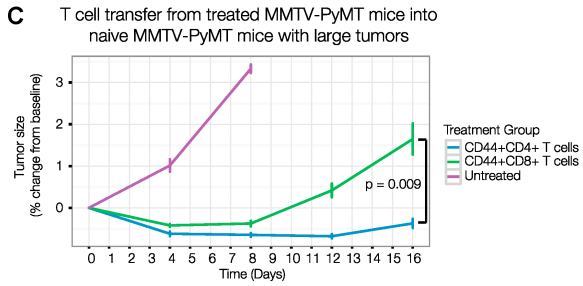

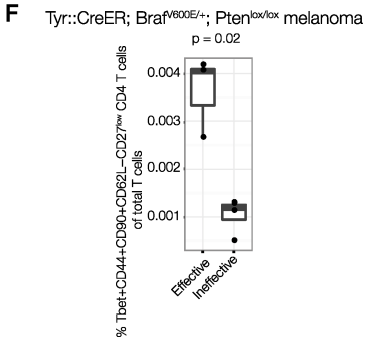

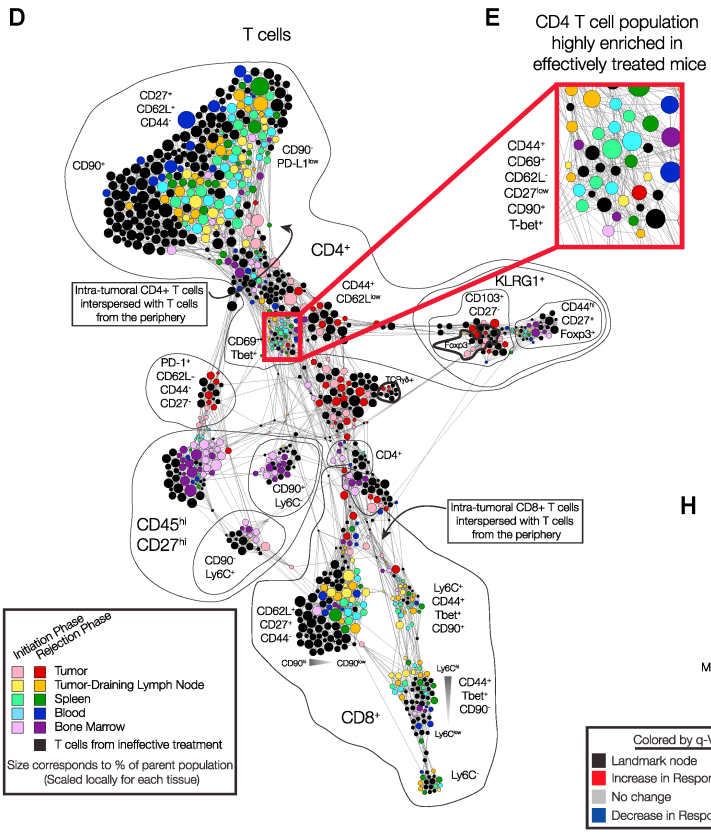

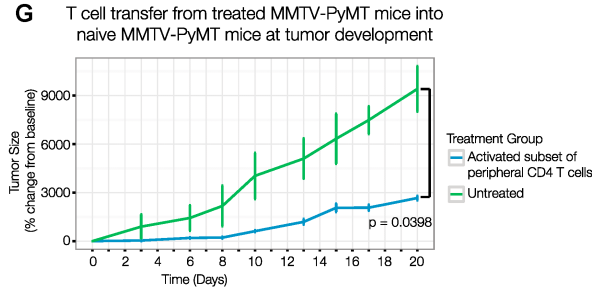

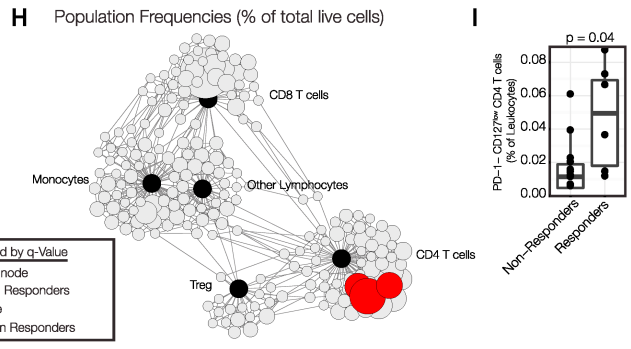

(legend on next page)

unique T cell phenotypes emerged after therapy, we performed an unsupervised clustering of all T cells across all tissues and visualized their similarities using a force-directed graph (Figure 6D). Each tissue was colored uniquely, with light colors representing cells from the priming phase and dark colors representing cells from the rejection phase. Cells from animals left untreated or treated with ineffective therapy are indicated in black in Figure 6D (with the inverted coloration in Figure S7D).

T cells from the tumor microenvironment occupied markedly distinct regions of the graph, denoting that these cells exhibited unique characteristics from cells in other organs. In contrast, cells from the draining lymph node, spleen, and blood were interspersed. Only animals treated with effective therapy contained T cells in the tumor similar to those from secondary lymphoid organs (Figure 6D). CD4 T cells in the periphery were mixed together by tissue but distinctly organized by treatment (Figure 6D). One region of the graph was highly enriched in cells from the periphery of mice receiving effective therapy (Figure 6E). The phenotype of these cells is most consistent with an activated, effector memory Th1 subset (CD44+CD69+CD62L−CD27^{low}T-bet+), and they uniquely expressed high levels of the immunoglobulin family member CD90 involved in T cell receptor signaling (Haeryfar and Hoskin, 2004). A similar subset also emerged after treatment in BP melanoma (Figure 6F).

We then tested whether this subset of CD4 T cells found in the periphery conferred tumor protection. These cells were sorted from the periphery of treated MMTV-PyMT mice and transferred into untreated animals at the time of tumorigenesis following sublethal irradiation. Indeed, this subset of peripheral CD4 T cells was capable of conferring significant protection against tumor development (Figure 6G). These results conclusively demonstrate that peripheral activated CD4 T cells are capable of orchestrating potent anti-tumor immunity.

A Similar CD4 T Cell Subset Is Associated with a Favorable Response to Immunotherapy in Melanoma Patients

We next determined whether similar CD4 T cells could be found in the blood of cancer patients who responded to immunotherapy. We recently described a clinical study of melanoma patients who received anti-CTLA-4 antibodies (Ipilimumab) in combination with GM-CSF (Kwek et al., 2015). We analyzed blood from these patients both three and six weeks post-therapy using Statistical Scaffold. Consistent with our pre-clinical results, specific clusters of CD4 T cells were significantly elevated in responders compared to non-responders at both time points (Figures 6H and S6E). A subset of Tregs was also elevated in responders 6 weeks after therapy (Figure S7E). The expanded clusters expressed lower levels of CD127 compared to the remaining CD4 T cells, indicative of activation, and lower levels of PD-1, suggesting that they were not exhausted (Figure S7F). We confirmed these results by manually gating PD-1-CD127^{low} CD4 T cells (Figure 6I). These results provide further experimental evidence of a critical role for CD4 T cells in coordinating effective anti-tumor immunity.

Simultaneous PD-L1 Blockade Breaks Tolerance to Uninjected Tumors in Multifocal Disease

We next asked whether we could leverage this modeling-based approach to improve the efficacy of the tumor-binding antibody therapy. An observation from the initial analysis is that many immune cells in the tumor significantly upregulate PD-L1 after the effective therapy (Figures 2B and 2C). PD-L1 is a repressor of T cell responses, and PD-L1 expression by tumor cells and immune cells mediates immunosuppression. We confirmed our observation by globally mapping cell subsets exhibiting significant differences in PD-L1 expression between therapies (Figure 7A). In the effectively treated animals, all myeloid cell subsets and some T cell subsets upregulated PD-L1 after effective therapy, as did tumor cells (Figure 7B). We hypothesized that PD-L1/PD-1 signaling may limit the efficacy of these immune responses. However, because these tumors do regress, a modified experimental setting was required to investigate this possibility.

MMTV-PyMT animals eventually develop tumors in all of their mammary fat pads. We had previously observed that, when animals were treated with tumor-binding antibody therapy after they had developed many tumors, only the injected tumor is rejected. In addition to the injected tumor, we also observed PD-L1 upregulation in the draining lymph node and blood (Figures 7C and 7D), as well as un-injected tumors during the priming phase

Figure 6. A CD4 T Cell Subset from the Periphery Is Sufficient to Mediate Anti-tumor Immunity

(A) Pairwise correlations and hierarchical clustering of immune cell frequencies across organs of mice treated with effective therapy.

(B) Adjacency matrix from (A) ordered by connectivity. CD4 T cells are indicated in black; CD8 T cells are indicated in white.

(C) CD44+ CD4 or CD8 T cells from the lymph node, spleen, and blood of MMTV-PyMT mice treated with effective therapy were expanded and transferred into treatment-naive MMTV-PyMT mice (n = 3–4 per group).

(D) Force-directed graph of T cells from each tissue, time, and treatment. Colored by tissue of origin. Light colors indicate initiation phase; dark colors indicate rejection phase. Clusters from mice receiving no or ineffective therapy are indicated in black. Node size reflects the frequency of T cells in that cluster as a percentage of T cells by tissue.

(E) CD4 T cells enriched in the periphery after effective therapy.

(F) Frequency of Tbet+CD44+CD62L−CD27^{low} CD4 T cells in the draining lymph node of mice with BP melanoma on day 8.

(G) CD44+CD62L−CD27^{low} CD4 T cells were isolated from the lymph node, spleen, and blood of MMTV-PyMT mice treated with effective therapy. Treatment-naive MMTV-PyMT mice were sublethally irradiated, and sorted T cells (n = 4) or PBS control (n = 3) was injected intravenously (i.v.). All p values reflect two-tailed, heteroskedastic t tests in R. Error bars represent SD.

(H) Scaffold map of flow cytometry data from blood of melanoma patients treated with anti-CTLA-4 antibodies and GM-CSF, 3 weeks after therapy began. Red nodes are cell subsets significantly expanded in responding patients compared to non-responders.

(I) Frequency of CD4+PD-1-CD127^{low} T cells (identified manually) of total leukocytes, analyzed by two-tailed Wilcoxon rank-sum test.

See also Figure S7.

Please cite this article in press as: Spitzer et al., Systemic Immunity Is Required for Effective Cancer Immunotherapy, Cell (2017), http://dx.doi.org/10.1016/j.cell.2016.12.022

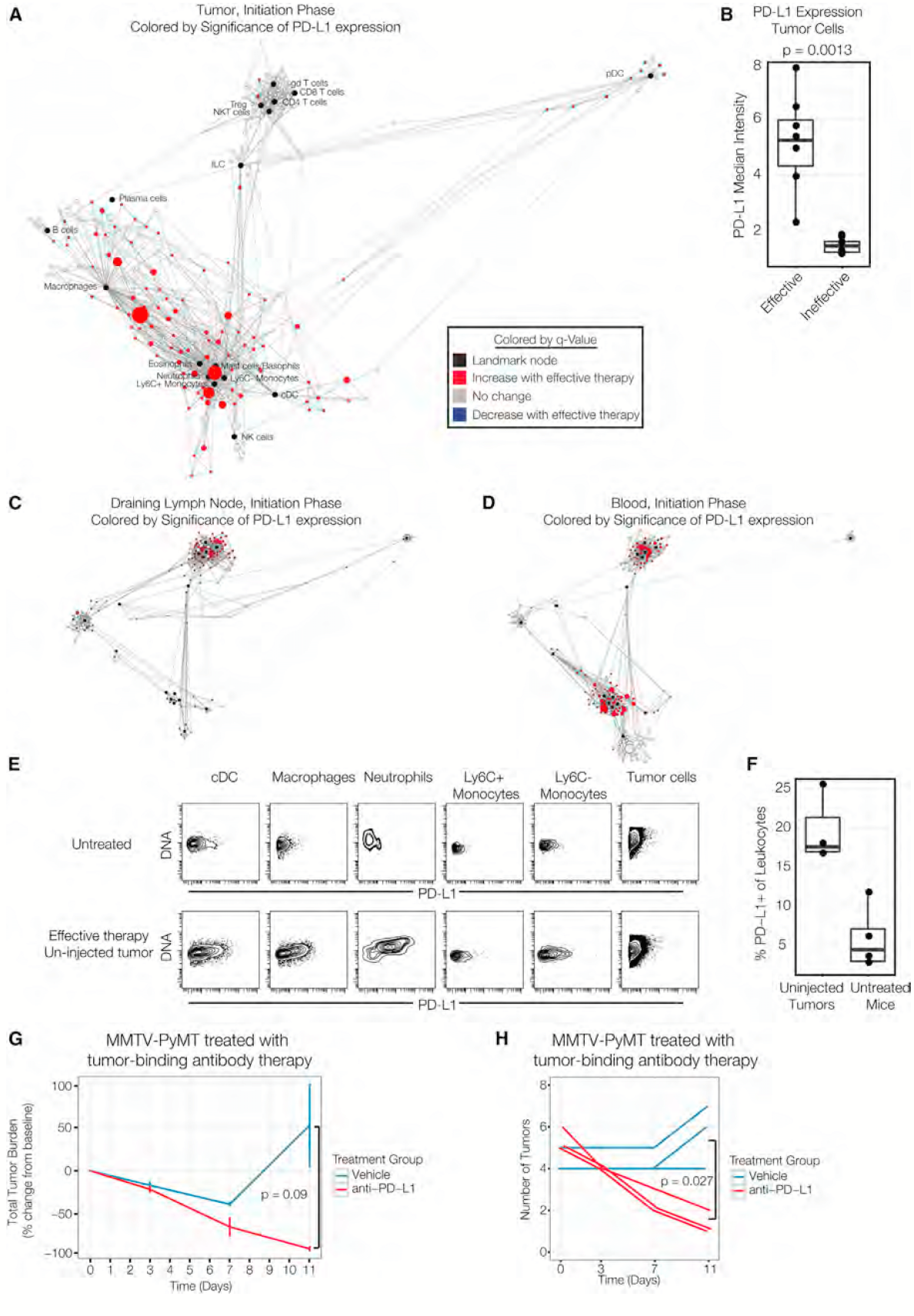

(legend on next page)

(Figures 7E and 7F). We hypothesized that the PD-L1/PD-1 axis may act more broadly to protect un-injected tumors.

We therefore asked whether systemic administration of anti-PD-L1 blocking antibodies might break tolerance to un-injected tumors. We treated MMTV-PyMT animals once they had developed many tumors with tumor-binding antibody therapy alone or in combination with anti-PD-L1. Combination with anti-PD-L1 resulted in additional reduction in overall tumor burden (Figure 7G) and rejection of multiple, un-injected tumors (Figure 7H). These results suggest that the PD-L1/PD-1 axis dampens the anti-tumor immune response to distal tumors, despite the systemic nature of the immune response.

DISCUSSION

The variance in clinical responses to immunotherapy suggests that productive immune responses against cancer are necessarily complex. There is an urgent need for methods to understand the nature of anti-tumor immunity to more reproducibly harness the immune system against cancer.

Here, we provide a systems-wide, organism-wide assessment of effective anti-tumor immune responses. Even for a therapy delivered intratumorally, a systemic immune response was required for tumor rejection. The effective tumor-binding antibody therapy activates a broad immune cell network including dendritic cells, which can prime T cells in the periphery. This could explain its efficacy against less immunogenic tumors compared to anti-PD-1, which is thought to act downstream on T cells themselves. With the increased use of immunotherapies, systemic responses should be taken into account when determining radiation or surgical regimens, including lymphadenectomy.

Our results indicate that secondary lymphoid organs are critical sites of T cell generation. This contrasts with results from a B16 melanoma model engineered to express strong model antigens, where intratumoral T cells could mediate rejection when combination immunotherapy was initiated early after tumor implantation (Spranger et al., 2014). While most adoptive T cell protocols utilize tumor-infiltrating cells (Rosenberg, 2014), a recent study has shown that T cells from blood can be used successfully (Cohen et al., 2015). While immune cells in the microenvironment may be sufficient in some settings, development of new immunotherapies must consider the benefit of systemic immunity.

Many studies have focused on CD8 T cells (Chen and Mellman, 2013; Im et al., 2016), with less emphasis on harnessing CD4 T cells (Tran et al., 2014; Xie et al., 2010). In other contexts, CD4 T cells orchestrate functional immune responses by coordinating immune activity (Swain et al., 2012). Our results extend this notion to anti-tumor immunity, providing a rationale for leveraging CD4 T cell responses in cancer.

These results highlight the benefit of system-wide assessments. Simple prognostic metrics have been proposed for monitoring anti-tumor immunity, including Treg frequency in tumors (Bates et al., 2006; Curiel et al., 2004). Productive immunity in this setting was accompanied by an increase in Treg frequency and proliferation in the context of a powerful T cell response. With high-throughput and high-dimensional single-cell technologies such as mass cytometry, assessing all immune cells simultaneously is now achievable, enabling individual metrics to be contextualized into the broader immune state. For instance, the systemic proliferative response identified may provide a means for noninvasive monitoring during immunotherapy. The graphical user interface that accompanies SCAFFoLD maps (https://github.com/nolanlab/scaffold/) enables further interrogation of this dataset. Using similar approaches, we expect that future studies will identify a multitude of drivers of effective responses.

A thorough understanding of the immune dynamics essential to any anti-tumor response requires comparison across numerous therapies. A systematic approach to understanding the mechanisms of new therapies will shed light on the core elements of immune activation required to reproducibly reject tumors. Additional behavioral programs, such as signaling, metabolism, and cytokine production, would enrich our view of the immune response.

These approaches also enabled rational design of drug combinations. PD-L1 induction mediated active resistance before T cells primed in the periphery could reach distal tumors, revealing another opportunity for modulating this pathway. System-wide studies should provide numerous opportunities for augmenting therapeutic efficacy.

The number of clinical trials in immunotherapy today provides opportunities to perform parallel studies in humans, building on our initial analysis here. A systematic understanding of anti-tumor immunity at the organismal and systems levels should enable significant progress in developing rational immunotherapeutic strategies.

STAR★METHODS

Detailed methods are provided in the online version of this paper and include the following:

- KEY RESOURCES TABLE
- CONTACT FOR REAGENT AND RESOURCE SHARING
- EXPERIMENTAL MODEL AND SUBJECT DETAILS

Figure 7. PD-L1 Blockade Combined with Tumor-Binding Antibody Therapy Enables Distal Tumor Rejection in Multifocal Disease

(A) Scaffold map denoting PD-L1 expression in immune cells in the tumor between effective and ineffective groups on day 3.

(B) Percentage of tumor cells expressing PD-L1 on day 3.

(C and D) Scaffold maps representing changes in PD-L1 expression in the (C) draining lymph node or (D) blood.

(E) PD-L1 expression in un-injected tumors in MMTV-PyMT mice with multi-focal disease on day 3.

(F) Frequency of PD-L1+ leukocytes in un-injected tumors of treated or untreated mice.

(G) Tumor burden in MMTV-PyMT animals with late-stage multi-focal disease after tumor-binding antibody therapy alone or in combination with systemic anti-PD-L1.

(H) Number of palpable tumors in mice from (G).

All p values reflect two-tailed, heteroskedastic t tests in R. Error bars represent SD.

SUPPLEMENTAL INFORMATION

Supplemental Information includes seven figures and three tables and can be found with this article online at http://dx.doi.org/10.1016/j.cell.2016.12.022.

AUTHOR CONTRIBUTIONS

Conceptualization, M.H.S., Y.C., and N.E.R.-F.; Experimental Methodology, M.H.S., Y.C., N.E.R.-F., S.S.K; Computational Methodology, M.H.S. and P.F.G.; Investigation, M.H.S., Y.C., N.E.R.-F., S.S.K., D.M., M.M.M., T.R.P., J.C., and L.F.; Writing – Original Draft, M.H.S.; Writing – Review & Editing, all authors; Funding Acquisition, M.H.S., S.C.B., L.F., G.P.N., and E.G.E.; Resources, S.C.B.; Supervision, L.F., G.P.N., and E.G.E.

ACKNOWLEDGMENTS

We thank G.K. Fragiadakis and L.E. Sanman for helpful conversations and feedback and A. Trejo and A. Jager for CyTOF maintenance. M.H.S., P.F.G., L.F., and G.P.N. are investigators of the Parker Institute for Cancer Immunotherapy. G.P.N. has a personal financial interest in, and S.C.B. has been a paid consultant for, Fluidigm, manufacturer of the mass cytometer utilized. E.G.E. is a founder and board member of Bolt Biotherapeutics, licensee of the therapy with alloIgG. This work was supported by NIH grants F31CA189331 and DP5OD023056 to M.H.S.; NIH grant F32CA189408 to N.R.F.; NIH grants U19AI057229, U19AI100627, R33CA183654, and R01HL120724, DOD grants OC110674 and 11491122, Gates Foundation grant OPP1113682, NIAID grant HHSN272201200028C, and FDA grant HHSF223201210194C BAA-12-00118 to G.P.N.; NIH grants R01CA196657 and U54CA209971 to G.P.N. and E.G.E.; and NIH grant R01AI118884 to E.G.E.

Received: June 16, 2016
Revised: October 27, 2016
Accepted: December 15, 2016
Published: January 19, 2017

REFERENCES

Bair, E., and Tibshirani, R. (2004). Semi-supervised methods to predict patient survival from gene expression data. PLoS Biol. *2*, E108.

Bandura, D.R., Baranov, V.I., Ornatsky, O.I., Antonov, A., Kinach, R., Lou, X., Pavlov, S., Vorobiev, S., Dick, J.E., and Tanner, S.D. (2009). Mass cytometry: technique for real time single cell multitarget immunoassay based on inductively coupled plasma time-of-flight mass spectrometry. Anal. Chem. *81*, 6813–6822.

Bastian, M., Heymann, S., and Jacomy, M. (2009). Gephi: an open source software for exploring and manipulating networks. International AAAI Conference on Weblogs and Social Media. http://www.aaai.org/ocs/index.php/ICWSM/09/paper/view/154/1009.

Bates, G.J., Fox, S.B., Han, C., Leek, R.D., Garcia, J.F., Harris, A.L., and Banham, A.H. (2006). Quantification of regulatory T cells enables the identification of high-risk breast cancer patients and those at risk of late relapse. J. Clin. Oncol. *24*, 5373–5380.

Bendall, S.C., Simonds, E.F., Qiu, P., Amir, A.D., Krutzik, P.O., Finck, R., Bruggner, R.V., Melamed, R., Trejo, A., Ornatsky, O.I., et al. (2011). Single-cell mass cytometry of differential immune and drug responses across a human hematopoietic continuum. Science *332*, 687–696.

Bos, P.D., Plitas, G., Rudra, D., Lee, S.Y., and Rudensky, A.Y. (2013). Transient regulatory T cell ablation deters oncogene-driven breast cancer and enhances radiotherapy. J. Exp. Med. *210*, 2435–2466.

Broz, M.L., Binnewies, M., Boldajipour, B., Nelson, A.E., Pollack, J.L., Erle, D.J., Barczak, A., Rosenblum, M.D., Daud, A., Barber, D.L., et al. (2014). Dissecting the tumor myeloid compartment reveals rare activating antigen-presenting cells critical for T cell immunity. Cancer Cell *26*, 638–652.

Bruggner, R.V., Bodenmiller, B., Dill, D.L., Tibshirani, R.J., and Nolan, G.P. (2014). Automated identification of stratifying signatures in cellular subpopulations. Proc. Natl. Acad. Sci. USA *111*, E2770–E2777.

Bulliard, Y., Jolicoeur, R., Windman, M., Rue, S.M., Ettenberg, S., Knee, D.A., Wilson, N.S., Dranoff, G., and Brogdon, J.L. (2013). Activating Fc γ receptors contribute to the antitumor activities of immunoregulatory receptor-targeting antibodies. J. Exp. Med. *210*, 1685–1693.

Carmi, Y., Spitzer, M.H., Linde, I.L., Burt, B.M., Prestwood, T.R., Perlman, N., Davidson, M.G., Kenkel, J.A., Segal, E., Pusapati, G.V., et al. (2015). Allogeneic IgG combined with dendritic cell stimuli induce antitumour T-cell immunity. Nature *521*, 99–104.

Chen, D.S., and Mellman, I. (2013). Oncology meets immunology: the cancer-immunity cycle. Immunity *39*, 1–10.

Cheng, G., Yuan, X., Tsai, M.S., Podack, E.R., Yu, A., and Malek, T.R. (2012). IL-2 receptor signaling is essential for the development of Klrg1+ terminally differentiated T regulatory cells. J. Immunol. *189*, 1780–1791.

Cohen, C.J., Gartner, J.J., Horovitz-Fried, M., Shamalov, K., Trebska-McGowan, K., Bliskovsky, V.V., Parkhurst, M.R., Ankri, C., Prickett, T.D., Crystal, J.S., et al. (2015). Isolation of neoantigen-specific T cells from tumor and peripheral lymphocytes. J. Clin. Invest. *125*, 3981–3991.

Coley, W.B. (1893). The treatment of malignant tumors by repeated inoculations of erysipelas. With a report of ten original cases. Am. J. Med. Sci. *105*, 487–511.

Corbett, T.H., Griswold, D.P., Roberts, B.J., Peckham, J.C., and Schabel, F.M. (1975). Tumor induction relationships in development of transplantable cancers of the colon in mice for chemotherapy assays, with a note on carcinogen structure. Cancer Research *35*, 2434–2439.

Curiel, T.J., Coukos, G., Zou, L., Alvarez, X., Cheng, P., Mottram, P., Evdemon-Hogan, M., Conejo-Garcia, J.R., Zhang, L., Burow, M., et al. (2004). Specific recruitment of regulatory T cells in ovarian carcinoma fosters immune privilege and predicts reduced survival. Nat. Med. *10*, 942–949.

Dankort, D., Curley, D.P., Cartlidge, R.A., Nelson, B., Karnezis, A.N., Damsky, W.E., Jr., You, M.J., DePinho, R.A., McMahon, M., and Bosenberg, M. (2009). Braf(V600E) cooperates with Pten loss to induce metastatic melanoma. Nat. Genet. *41*, 544–552.

Finck, R., Simonds, E.F., Jager, A., Krishnaswamy, S., Sachs, K., Fantl, W., Pe'er, D., Nolan, G.P., and Bendall, S.C. (2013). Normalization of mass cytometry data with bead standards. Cytometry A *83*, 483–494.

Gabrilovich, D.I., Ostrand-Rosenberg, S., and Bronte, V. (2012). Coordinated regulation of myeloid cells by tumours. Nat. Rev. Immunol. *12*, 253–268.

Haeryfar, S.M.M., and Hoskin, D.W. (2004). Thy-1: more than a mouse pan-T cell marker. J. Immunol. *173*, 3581–3588.

Hänninen, A., Maksimow, M., Alam, C., Morgan, D.J., and Jalkanen, S. (2011). Ly6C supports preferential homing of central memory CD8+ T cells into lymph nodes. Eur. J. Immunol. *41*, 634–644.

Herbst, R.S., Soria, J.-C., Kowanetz, M., Fine, G.D., Hamid, O., Gordon, M.S., Sosman, J.A., McDermott, D.F., Powderly, J.D., Gettinger, S.N., et al. (2014). Predictive correlates of response to the anti-PD-L1 antibody MPDL3280A in cancer patients. Nature *515*, 563–567.

Hotson, A.N., Gopinath, S., Nicolau, M., Khasanova, A., Finck, R., Monack, D., and Nolan, G.P. (2016). Coordinate actions of innate immune responses oppose those of the adaptive immune system during Salmonella infection of mice. Sci Signal *12*, ra4.

Ideker, T., and Krogan, N.J. (2012). Differential network biology. Mol. Syst. Biol. *8*, 565.

Im, S.J., Hashimoto, M., Gerner, M.Y., Lee, J., Kissick, H.T., Burger, M.C., Shan, Q., Hale, J.S., Lee, J., Nasti, T.H., et al. (2016). Defining CD8(+) T cells that provide the proliferative burst after PD-1 therapy. Nature *537*, 417–421.

Jiang, Y., Li, Y., and Zhu, B. (2015). T-cell exhaustion in the tumor microenvironment. Cell Death Dis. *6*, e1792.

Kantoff, P.W., Higano, C.S., Shore, N.D., Berger, E.R., Small, E.J., Penson, D.F., Redfern, C.H., Ferrari, A.C., Dreicer, R., Sims, R.B., et al.; IMPACT Study Investigators (2010). Sipuleucel-T immunotherapy for castration-resistant prostate cancer. N. Engl. J. Med. *363*, 411–422.

Kvistborg, P., Philips, D., Kelderman, S., Hageman, L., Ottensmeier, C., Joseph-Pietras, D., Welters, M.J.P., van der Burg, S., Kapiteijn, E., Michielin, O., et al. (2014). Anti-CTLA-4 therapy broadens the melanoma-reactive CD8+ T cell response. Sci. Transl. Med. *6*, 254ra128.

Kwek, S.S., Kahn, J., Greaney, S.K., Lewis, J., Cha, E., Zhang, L., Weber, R.W., Leonard, L., Markovic, S.N., Fong, L., and Spitler, L.E. (2015). GM-CSF and ipilimumab therapy in metastatic melanoma: Clinical outcomes and immunologic responses. OncoImmunology *5*, e1101204–e1101211.

Matloubian, M., Lo, C.G., Cinamon, G., Lesneski, M.J., Xu, Y., Brinkmann, V., Allende, M.L., Proia, R.L., and Cyster, J.G. (2004). Lymphocyte egress from thymus and peripheral lymphoid organs is dependent on S1P receptor 1. Nature *427*, 355–360.

Pelletier, N., McHeyzer-Williams, L.J., Wong, K.A., Urich, E., Fazilleau, N., and McHeyzer-Williams, M.G. (2010). Plasma cells negatively regulate the follicular helper T cell program. Nat. Immunol. *11*, 1110–1118.

Porter, D.L., Levine, B.L., Kalos, M., Bagg, A., and June, C.H. (2011). Chimeric antigen receptor-modified T cells in chronic lymphoid leukemia. N. Engl. J. Med. *365*, 725–733.

Restifo, N.P., Dudley, M.E., and Rosenberg, S.A. (2012). Adoptive immunotherapy for cancer: harnessing the T cell response. Nat. Rev. Immunol. *12*, 269–281.

Rosenberg, S.A. (2014). Decade in review-cancer immunotherapy: entering the mainstream of cancer treatment. Nat. Rev. Clin. Oncol. *11*, 630–632.

Simpson, T.R., Li, F., Montalvo-Ortiz, W., Sepulveda, M.A., Bergerhoff, K., Arce, F., Roddie, C., Henry, J.Y., Yagita, H., Wolchok, J.D., et al. (2013). Fc-dependent depletion of tumor-infiltrating regulatory T cells co-defines the efficacy of anti-CTLA-4 therapy against melanoma. J. Exp. Med. *210*, 1695–1710.

Spitzer, M.H., Gherardini, P.F., Fragiadakis, G.K., Bhattacharya, N., Yuan, R.T., Hotson, A.N., Finck, R., Carmi, Y., Zunder, E.R., Fantl, W.J., et al. (2015). IMMUNOLOGY. An interactive reference framework for modeling a dynamic immune system. Science *349*, 1259425.

Spranger, S., Koblish, H.K., Horton, B., Scherle, P.A., Newton, R., and Gajewski, T.F. (2014). Mechanism of tumor rejection with doublets of CTLA-4, PD-1/PD-L1, or IDO blockade involves restored IL-2 production and proliferation of CD8(+) T cells directly within the tumor microenvironment. J. Immunother. Cancer *2*, 3.

Swain, S.L., McKinstry, K.K., and Strutt, T.M. (2012). Expanding roles for $CD4^+$ T cells in immunity to viruses. Nat. Rev. Immunol. *12*, 136–148.

Topalian, S.L., Drake, C.G., and Pardoll, D.M. (2015). Immune checkpoint blockade: a common denominator approach to cancer therapy. Cancer Cell *27*, 450–461.

Tran, E., Turcotte, S., Gros, A., Robbins, P.F., Lu, Y.-C., Dudley, M.E., Wunderlich, J.R., Somerville, R.P., Hogan, K., Hinrichs, C.S., et al. (2014). Cancer immunotherapy based on mutation-specific CD4+ T cells in a patient with epithelial cancer. Science *344*, 641–645.

Wherry, E.J., Ha, S.-J., Kaech, S.M., Haining, W.N., Sarkar, S., Kalia, V., Subramaniam, S., Blattman, J.N., Barber, D.L., and Ahmed, R. (2007). Molecular signature of CD8+ T cell exhaustion during chronic viral infection. Immunity *27*, 670–684.

Xie, Y., Akpinarli, A., Maris, C., Hipkiss, E.L., Lane, M., Kwon, E.-K.M., Muranski, P., Restifo, N.P., and Antony, P.A. (2010). Naive tumor-specific CD4(+) T cells differentiated in vivo eradicate established melanoma. J. Exp. Med. *207*, 651–667.

Zunder, E.R., Finck, R., Behbehani, G.K., Amir, A.D., Krishnaswamy, S., Gonzalez, V.D., Lorang, C.G., Bjornson, Z., Spitzer, M.H., Bodenmiller, B., et al. (2015). Palladium-based mass tag cell barcoding with a doublet-filtering scheme and single-cell deconvolution algorithm. Nat. Protoc. *10*, 316–333.

Please cite this article in press as: Spitzer et al., Systemic Immunity Is Required for Effective Cancer Immunotherapy, Cell (2017), http://dx.doi.org/10.1016/j.cell.2016.12.022

STAR★METHODS

KEY RESOURCES TABLE

REAGENT or RESOURCE	SOURCE	IDENTIFIER
Antibodies		
Mass cytometry antibodies are found in Table S1.	This paper	N/A
Rat anti-mouse CD40, clone FGK4.5	BioXCell	Cat#BE0016-2; RRID: AB_1107647
Rat anti-mouse PD-L1, clone 10F.9G2	BioXCell	Cat#BE0101; RRID: AB_10949073
Rat anti-mouse PD-1, clone RMP1-14	BioXCell	Cat# BE0146
Biological Samples		
Serum from C57BL/6 retired breeders	Charles River	N/A
Serum from CD-1 retired breeders	Charles River	N/A
Chemicals, Peptides, and Recombinant Proteins		
Recombinant mouse interferon-γ	Biolegend	Cat#575302
Recombinant human IL-2	Peprotech	Cat#200-02
FTY720 (Fingolimod)	Cayman Chemical	Cat#10006292
Critical Commercial Assays		
Mass cytometry antibody conjugation kits	Fluidigm	Cat#201300
HiTrap Protein G HP columns	GE Healthcare	Cat#17-0404-01
Deposited Data		
Mass cytometry data	This paper	https://github.com/spitzerlab/Modeling_Effective_Cancer_Immunotherapy
Experimental Models: Cell Lines		
4T1 breast carcinoma cells	ATCC	Cat#CRL-2539
MC38 colon carcinoma cells	Corbett et al., 1975	RRID:CVCL_B288
Experimental Models: Organisms/Strains		
Mouse: FVB/N-Tg(MMTV-PyVT)634Mul/J	Jackson Laboratory	Cat#002374
Mouse: B6.Cg-Braftm1Mmcm Ptentm1Hwu Tg(Tyr-cre/ERT2)13Bos/BosJ	Jackson Laboratory	Cat#013590
Software and Algorithms		
Statistical Scaffold	This paper	https://github.com/spitzerlab/Modeling_Effective_Cancer_Immunotherapy
Scaffold Maps (as originally implemented)	Spitzer et al., 2015	http://www.github.com/nolanlab/scaffold/
Gephi	Bastian et al., 2009	https://gephi.org

CONTACT FOR REAGENT AND RESOURCE SHARING

Further information and requests for resources and reagents should be directed to and will be fulfilled by Lead Contact Matthew Spitzer (matthew.spitzer@ucsf.edu).

EXPERIMENTAL MODEL AND SUBJECT DETAILS

Animals

Female MMTV-PyMT mice and male Tyr::CreER; *Braf*$^{V600E/+}$; *Pten*$^{lox/lox}$ mice were bred in our colony at Stanford University. All mice were housed in an American Association for the Accreditation of Laboratory Animal Care–accredited animal facility and maintained in specific pathogen-free conditions. Animal experiments were approved and conducted in accordance with Stanford University Asia Pacific Laboratory Accreditation Cooperation #13605. Animals began treatment when they developed a primary tumor reaching 25mm^2 in area (referred to as day 0) and were randomized to different treatment groups. Wild-type female FVB, BALB/c or C57BL/6 mice were purchased from The Jackson Laboratory and housed at our facility or were bred at Stanford University. Mice were transplanted with 2.5 × 10^5 tumor cells when the mice were nine to twelve weeks of age. 4T1 breast cancer cells were

transplanted into the fourth mammary fat pad, and MC38 cells were transplanted into the subcutaneous region of the flank when animals were between 8-10 weeks old. Animals were housed under standard SPF conditions with typical light/dark cycles and standard chow.

Human Subjects

Eligible patients were adults with histologically confirmed unresectable metastatic melanoma as previously reported (Kwek et al., 2015). The protocol was approved by the Institutional Review Board of each participating institution and was conducted in accordance with the ethical principles of the Declaration of Helsinki and within the Good Clinical Practice guidelines as defined by the International Conference on Harmonization. All patients gave written informed consent for participation in the study. The trial was registered on ClinicalTrials.gov with Identifier NCT01363206.

At the initiation of treatment (months 1–3), patients were treated with four cycles of GM-CSF and ipilimumab administered every 3 weeks. Ipilimumab was administered intravenously at a dose of 10 mg/kg on day 1 of each 21 d cycle. GM-CSF was administered subcutaneously daily for 14 d at a dose of 125 mg/m^2 beginning on day 1 of each cycle. After the first four cycles of treatment, GM-CSF administration without ipilimumab continued for four more cycles on the same schedule and dose for the first 14 d of every 21 d cycle until month 6. Maintenance therapy began at month 6 and consisted of ipilimumab in the same dose (10 mg/kg) combined with 14 d of GM-CSF. This combination was administered every 3 mo thereafter for up to 2 y or until disease progression or unacceptable toxicity. Blood samples were obtained at week 3 (end of cycle 1) and at week 6 (end of cycle 2) and were cryopreserved for subsequent analysis by flow cytometry.

Cell Lines

4T1 cells were purchased from the ATCC (catalog number CRL-2539). 4T1 and MC38 cells were cultured in RPMI-1640 supplemented with 10% FCS, 2 mM L-glutamine,100 U/mL penicillin and 100 μg/mL penicillin/streptomycin.

Primary Cell Cultures

MMTV-PyMT T Cell Transfer Studies

MMTV-PyMT animals bearing 25mm^2 tumors were treated with anti-CD40, IFNγ, and allogeneic (CD-1) IgG antibodies as described under "Treatments." On day 7 following treatment, mice were euthanized and their spleens and lymph nodes harvested. Following tissue dissociation, T cells were enriched using the EasySep Mouse T Cell Enrichment Kit (StemCell, 588CAD), and sorted by FACS for the following markers: CD4+CD69+CD44+Lin- or CD8a+Ly6C+CD44+Lin-. Cells were expanded in vitro by culturing in RPMI-1640 supplemented with 10% FCS, 2 mM L-glutamine,100 U/mL penicillin, 100 μg/mL penicillin/streptomycin, 30IU of hIL-2 and anti-CD3/CD28 Dynabeads (Life Technologies, 11452D) at a bead:cell ratio of 1:2. Cells were expended with beads for 7 days, after which the beads were removed and the cells were cultured for an additional two days. Tumor-bearing naive MMTV-PyMT recipient mice were sub-lethally irradiated with 4 Gray. Subsequently, 3x10^6 CD4 or CD8 T cell populations were transferred to the mice through tail vein injections in 200 μL of PBS. Tumor burden was assessed on days 0, 4, 8, 12, and 16 following T cell transfer.

METHOD DETAILS

Tumor-Binding Antibody Purification

Mouse antibodies were obtained from the pooled sera of retired breeders from Charles River using protein-G columns (GE Healthcare). The levels of purified IgG and were measured using a NanoDrop spectrophotometer (Thermo Scientific). The capacity of purified antibodies to bind tumor cells was tested by flow cytometry before their use in vivo.

Treatments

Animals treated for tumor kinetics analysis were injected intratumorally with 100 μg anti-CD40 (clone FGK4.5; BioXCell) and 1 μg IFNγ (Biolegend) with or without 300 μg B6 IgG antibodies and 300 μg CD-1 IgG antibodies. Animals treated for mass cytometry analysis with tumor-binding antibody therapy were injected intratumorally with 400 μg allo-IgG (either B6 or CD-1) and 100 μg anti-CD40 and IFNγ or with 250 μg anti-PD-1 (clone RMP1-14, BioXCell) injected i.p. Injections were performed on day 0 and day 2. In some cases, mice were injected i.p. with 200 μg of anti-PD-L1 (clone 10F.9G2; BioXCell) every 3 days until the experiment was terminated. Day 0 was considered the first day of treatment.

Mass Cytometry Antibodies

A summary of all mass cytometry antibodies, reporter isotopes and concentrations used for analysis can be found in Table S1. Primary conjugates of mass cytometry antibodies were prepared using the MaxPAR antibody conjugation kit (Fluidigm) according to the manufacturer's recommended protocol. Following labeling, antibodies were diluted in Candor PBS Antibody Stabilization solution (Candor Bioscience GmbH, Wangen, Germany) supplemented with 0.02% NaN_3 to between 0.1 and 0.3 mg/mL and stored long-term at 4°C. Each antibody clone and lot was titrated to optimal staining concentrations using primary murine samples. One antibody cocktail was prepared for the staining of all samples for mass cytometry analysis.

Please cite this article in press as: Spitzer et al., Systemic Immunity Is Required for Effective Cancer Immunotherapy, Cell (2017), http://dx.doi.org/10.1016/j.cell.2016.12.022

Cell Preparation

All tissue preparations were performed simultaneously from each individual mouse. After euthanasia by $C0_2$ inhalation, peripheral blood was collected via the posterior vena cava prior to perfusion of the animal and transferred into sodium heparin-coated vacuum tubes prior to 1:1 dilution in RMPI 1640. Spleens and lymph nodes were homogenized in PBS + 5mM EDTA at 4°C. Bone marrow was flushed from femuri and resuspended in PBS + 5mM EDTA at 4°. Tumors were finely minced and digested in RPMI 1640 with 1 mg/ml collagenase IV, and 0.1 mg/ml DNase I. After digestion, cells re-suspended cells were quenched with RPMI with 10% FCS at 4°C. Cells were then homogenized in RPMI with 10% FCS. All tissues except peripheral blood were washed with PBS with 5mM EDTA and resuspended 1:1 with PBS with 5mM EDTA and 100 μM Ciaplatin (Enzo Life Sciences, Farmingdale, NY) for 60 s before quenching 1:1 with PBS with 0.5% BSA and 5mM EDTA to determine viability as previously described (Spitzer et al., 2015). Cells were centrifuged at 500 g for 5 min at 4°C and resuspended in PBS with 0.5% BSA and 5mM EDTA at a density between 1-10*10^6 cells/ml. Suspensions and blood were fixed for 10 min at RT using 1:1.4 Proteomic Stabilizer according to the manufacturer's instructions (Smart Tube Inc., Palo Alto, CA) and frozen at −80°C.

Mass-Tag Cellular Barcoding

Mass-tag cellular barcoding was performed as previously described (Zunder et al., 2015). Briefly, 1*10^6 cells from each animal were barcoded with distinct combinations of stable Pd isotopes chelated by isothiocyanobenzyl-EDTA in 0.02% saponin in PBS. Samples from any given tissue from one mouse per treatment group were barcoded together, with at least 3 biological replicates per treatment group across different plates. Cells were washed two times in PBS with 0.5% BSA and 0.02% NaN3 and pooled into a single FACS tube (BD Biosciences). After data collection, each condition was deconvoluted using a single-cell debarcoding algorithm (Zunder et al., 2015).

Mass Cytometry Staining and Measurement

Cells were resuspended in PBS with 0.5% BSA and 0.02% NaN_3 and metal-labeled antibodies against CD16/32 were added at 20 μg/ml for 5 min at RT on a shaker to block Fc receptors. Surface marker antibodies were then added, yielding 500 uL final reaction volumes and stained at room temperature for 30min at RT on a shaker. Following staining, cells were washed 2 more times with PBS with 0.5% BSA and 0.02% NaN3 then permeabilized with 4°C methanol for at 10 min at 4°C. Cells were then washed twice in PBS with 0.5% BSA and 0.02% NaN_3 to remove remaining methanol, and then stained with intracellular antibodies in 500 μL for 30 min at RT on a shaker. Cells were washed twice in PBS with 0.5% BSA and 0.02% NaN_3 and then stained with 1 mL of 1:4000 191/193Ir DNA intercalator (Fluidigm) diluted in PBS with 1.6% PFA overnight. Cells were then washed once with PBS with 0.5% BSA and 0.02% NaN_3 and then two times with double-deionized (dd)H20. Care was taken to assure buffers preceding analysis were not contaminated with metals in the mass range above 100 Da. Mass cytometry samples were diluted in ddH2O containing bead standards (see below) to approximately 106 cells per mL and then analyzed on a CyTOF 2 mass cytometer (Fluidigm) equilibrated with ddH_2O. We analyzed 1-5*10^5 cells per animal, per tissue, per time point, per treatment, consistent with generally accepted practices in the field.

Bead Standard Data Normalization

Just before analysis, the stained and intercalated cell pellet was resuspended in ddH_2O containing the bead standard at a concentration ranging between 1 and 2*10^4 beads per ml as previously described (Finck et al., 2013). The bead standards were prepared immediately before analysis, and the mixture of beads and cells were filtered through a filter cap FACS tubes (BD Biosciences) before analysis. All mass cytometry files were normalized together using the mass cytometry data normalization algorithm (Finck et al., 2013), which uses the intensity values of a sliding window of these bead standards to correct for instrument fluctuations over time and between samples.

Scaffold Map Generation

Total live leukocytes (excluding erythrocytes) were used for all analyses. Cells from each tissue for all animals were clustered together (rather than performing CLARA clustering on each file individually as originally implemented in Spitzer et al., 2015.) Cells were then deconvolved into their respective samples. Cluster frequencies or the Boolean expression of Ki67 or PD-L1 for each cluster were passed into the Significance Across Microarrays algorithm (Bair and Tibshirani, 2004; Bruggner et al., 2014), and results were tabulated into the Scaffold map files for visualization through the graphical user interface. Cluster frequencies were calculated as a percent of total live nucleated cells (excluding erythrocytes). For each cluster in each tissue, the most similar cluster in every other tissue is included as Table S3 for comparisons.

Scaffold maps were then generated as previously reported (Spitzer et al., 2015). Briefly, we chose the spleen data to spatialize the initial Scaffold map because all major, mature immune cell populations are present in that tissue. A graph was constructed by first connecting together the nodes representing the manually gated landmark populations and then connecting to them the nodes representing the cell clusters as well as connecting the clusters to one another. Each node is associated with a vector containing the median marker values of the cells in the cluster (unsupervised nodes) or gated populations (landmark nodes). Edge weights were defined as the cosine similarity between these vectors after comparing the results from the implementation of several distance metrics. Edges of low weight were filtered out. We experimented with different threshold values for the weights and we found values of

0.8 for the initial subgraph of landmark nodes, and 0.7 for the complete graph to produce satisfying results. The graph was then laid out using an in-house R implementation of the ForceAtlas2 algorithm from the graph visualization software Gephi. To overlay the additional samples on the spleen map, the position and identity of the landmark nodes was fixed and the clusters of each sample were connected to the landmark nodes as described above. Once again the graphs were laid out using ForceAtlas2 but this time only the unsupervised nodes were allowed to move. All analyses were performed using the open source Scaffold maps R package available at http://www.github.com/nolanlab/scaffold.

Cell Population Expression Profiles

Cell clusters of interest were further investigated by visualizing the distribution of protein expression within the cells comprising each cluster as a histogram. This was performed using the density visualization feature of the Scaffold maps R package. Histograms shown in the figures were created by exporting clusters as. FCS files using the Scaffold maps R package and using the flowCore and ggplot2 packages in R to write vector histogram plots. Scripts are available at http://www.github.com/mhspitzer.

Unsupervised Force-Directed Graph Generation

Cells were manually gated as Live CD45+ lineage- (Ter119, Ly6G, Siglec-F, CD19, B220, F4/80, CD11c, PDCA-1, FcεR1α) and then CD3+ to identify T cells. The gated cell populations for each tissue/time point/treatment group were clustered independently in 50 clusters using clara in R. The clusters for all the tissues were combined in a single graph with edge weights defined as the cosine similarity between the vectors of median marker values of each cluster. All the pairwise distances were calculated and for each node only the 10 edges of highest weight were retained. The graph was then laid out using the ForceAtlas2 algorithm in Gephi (https://gephi.org).

Correlation Network Analysis and Connectivity Analysis

Immune cell subsets were gated from mass cytometry data, and the frequency of each subset in each tissue of each mouse was calculated. For animals receiving effective therapy or those receiving no or ineffective therapy, pairwise Spearman correlations were calculated for each immune cell subset, and hierarchical clustering was performed to organize the correlation matrix. The hierarchical clustering result from the mice receiving effective therapy was additionally imposed on the correlation matrix for the animals receiving no or ineffective therapy as a means of comparing the networks.

For the connectivity analysis, an adjacency matrix was created from the correlation matrix of animals receiving effective therapy, using a Spearman correlation coefficient of 0.5 as the threshold. The number of remaining correlations was tabulated for each immune cell population from each tissue, and these were rank ordered. The graph of the adjacency matrix visualizes all positive and negative correlations present in the adjacency matrix for each subset.

Histology and Immunohistochemistry

Following excision from mice, tissues were fixed in 4% buffered formalin for one hour at room temperature. Tissues were then transferred to 30% sucrose solution in PBS and left overnight at 4°C. They were then embedded in O.C.T. Compound (Tissue-Tek) and frozen on dry ice. Tissue blocks were sectioned at 6 μm on a microtome onto positively charged glass slides (Fisher Scientific) and stained with Hematoxylin and Eosin (H&E) according to standard protocols.

Additional slides were blocked with PBS containing 10% normal goat serum and 5% BSA for 30 min at room temperature and stained for the following antigens at a 1:100 dilution overnight at 4°C: CD45 (30-F11, BioLegend), CD8α (53-6.7, BioLegend), CD4 (RM4-5, BioLegend), and CD11b (M1/70, BioLegend), mounted with LabVision PermaFluor Aqueous Mounting Medium (Thermo Scientific), and imaged on a Zeiss LSM700 confocal microscope.

When co-stained with TUNEL, sections were stained overnight at 4°C with 1:50 dilution of rat-anti mouse polyoma virus- middle T antigen (Santa Cruz Biotechnology). Sections were then washed three times in PBS, incubated for 1 hr at room temperature with, and stained with 1:100 Alexa Fluor 647-conjugated anti-CD8β (YTS156.7.7) and with 1:200 Alexa Fluor 488-Conjugated anti-rat IgG antibodies (BioLegend). Terminal deoxynucleotidyl transferase–mediated dUTP nick end labeling (TUNEL) assays were performed according to manufacturer's instructions (Roche manual). Briefly, cells were washed thrice in PBS, and fixed in freshly prepared 4% paraformaldehyde in PBS for 1 hr at room temperature, and then washed with PBS and permeabilized in 0.1% Triton X-100 in 0.1% sodium citrate. Cells were then incubated with TUNEL reaction mixture (Roche) for 60 min at 37°C in a humidified atmosphere in the dark.

Leukocyte Egress Blockade

Animals bearing 25mm^2 tumors were treated with alloIgG (from B6 mice), anti-CD40 and IFNγ and were randomized to receive daily i.p. injections of FTY720 (3 mg/kg) or ethanol control beginning one day prior to therapy.

Adoptive T Cell Transfer

BALB/c mice were injected orthotopically into the fourth mammary fat pad with 10^5 4T1 tumor cells. On days 12 and 14, mice were injected intratumorally with 100 μg anti-CD40 (clone FGK4.5; BioXCell) and 1 μg IFNγ (Biolegend) and 400 μg allo-IgG along with daily i.p. injections of FTY720 (3mg/kg). On day seven, mice were euthanized and the draining lymph nodes and spleens were removed and mechanically dissociated to obtain single cell suspension. T cells were then enriched by negative selection using magnetic beads

(EasySep, StemCell technologies) and a total of $8x10^6$ cells were injected intravenously into BALB/c female mice. After one day, both T cell-recipient mice and naive control mice were challenged with $5x10^4$ 4T1 tumor cells subcutaneously. Starting the day of T cell transfer, mice were treated twice a day for five days with 220,000 IU of human IL-2 (Peprotech).

Flow Cytometry

For human samples, cell surface staining was performed in fluorescence-activated cell sorting (FACS) buffer for 30 min at 4°C. Intracellular foxhead box P3 (FoxP3) was performed using the FoxP3 fix/perm buffer set (Biolegend, Inc.) according to the manufacturer's protocol. The following anti-human antibodies were used: (Alexa Fluor 700)-CD3 (clone HIT3a), (Brilliant violet 570)-CD4 (clone RPA-T4), (Brilliant violet 650)-CD25 (clone BC96), (Alexa Fluor 647)-CD127 (clone A019D5), (Alexa Fluor 488)-FoxP3 (clone 206D), and (Brilliant violet 421)-PD-1 (clone EH12.2H7). All antibodies were purchased from Biolegend, Inc. Stained cells were fixed with Fluorofix buffer (Biolegend, Inc.) according to manufacturer's instructions and analyzed with an LSR II flow cytometer (BD Biosciences).

QUANTIFICATION AND STATISTICAL ANALYSIS

Comparison of cell frequencies and protein expression in Statistical Scaffold was performed using Significance Analysis of Microarrays as described above and in Bair and Tibshirani, 2004 and Bruggner et al., 2014. Individual comparisons presented as stand-alone panels were made using heteroskedastic, two-tailed t tests performed in R.

Analysis of tumor sizes was performed by calculating a fold change in the size of the tumor at time point *t* compared to the baseline size at the time of treatment or adoptive transfer. Comparisons were made using heteroskedastic, two-tailed t tests performed in R.

Frequency of human CD4+PD-1-CD127^{low} T cells (identified manually) was calculated as a percent of total leukocytes, and results were compared between responding and non-responding patients by two-tailed Wilcoxon rank-sum test performed in R.

DATA AND SOFTWARE AVAILABILITY

Statistical Scaffold and all mass cytometry data are publicly available at http://www.github.com/spitzerlab/Modeling_Effective_Cancer_Immunotherapy/.

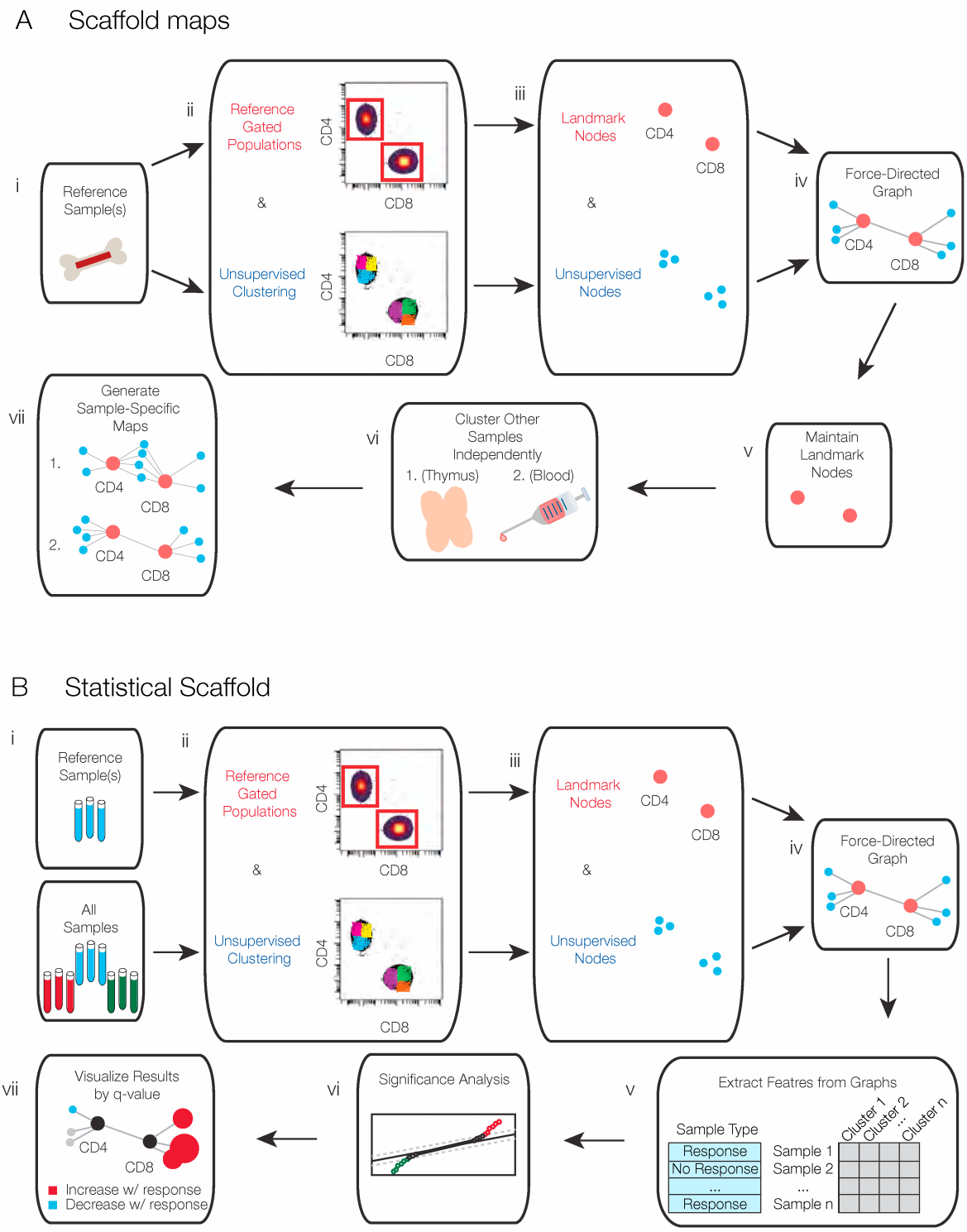

Figure S1. The Statistical Scaffold Algorithm, Related to Figure 1

(A) Scaffold maps as originally designed (Spitzer et al., 2015). (i) A reference sample (or group thereof) is chosen for the analysis. (ii) Canonical cell populations are identified manually and all cells are also clustered in an unsupervised manner. (iii) Canonical populations are represented as landmark nodes, while clusters are represented as unsupervised nodes. (iv) These nodes are spatialized into a force-directed graph. (v) Landmark nodes are fixed in place to provide common reference points. (vi) Cells from other samples are clustered independently and (viii) graphs are generated for each sample. (B) Statistical Scaffold. (i-ii) A set of reference samples is chosen and canonical cell populations as performed previously. However, all samples are clustered together. (iii-iv) Same as above. (v) Features (i.e., population frequencies, expression levels in each cluster, etc.) are extracted from the clusters for each

(legend continued on next page)

sample. Each sample is also annotated according to the therapy to which it belongs. (vi) Significance Analysis of Microarrays is performed to identify features that are statistically significant between treatment groups. (vii) Features displaying statistically significant differences between groups are colored according to the direction of the change (increase or decrease) in the Scaffold maps to visualize which parts of the immune system are impacted by therapy.

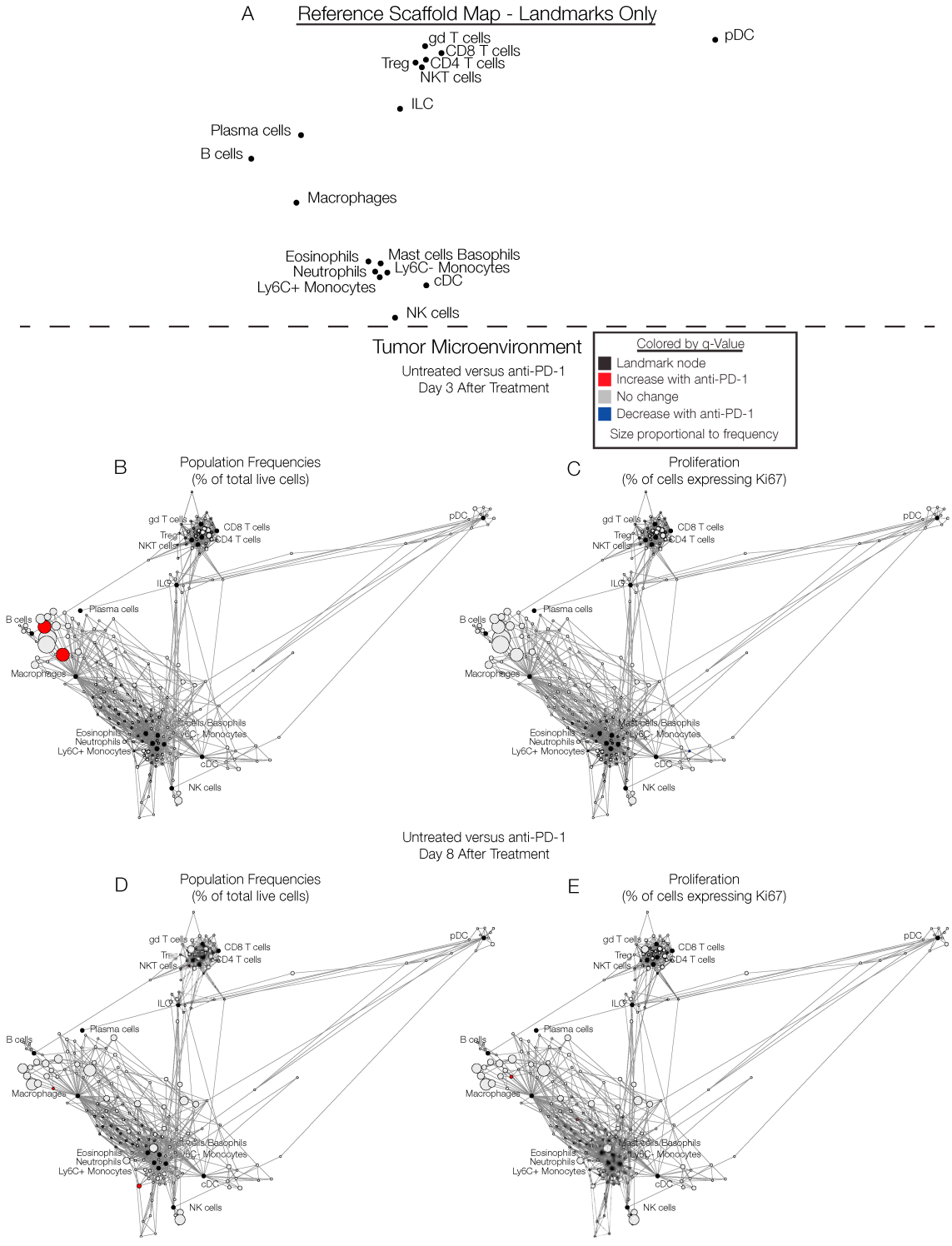

Figure S2. Architecture of the Scaffold Map, Related to Figure 2

(A) An empty Scaffold map displaying landmarks alone is presented here for assistance when reading the primary figures. (B) Statistical Scaffold map showing differences in immune cell population frequencies in the tumor microenvironment of animals 3 days after treatment with anti-PD-1 antibodies or left untreated. (C) Statistical Scaffold map showing differences in immune cell proliferation (Ki67 expression) in the tumor microenvironment of animals 3 days after treatment with anti-PD-1 antibodies or left untreated. (D) Statistical Scaffold map showing differences in immune cell population frequencies in the tumor microenvironment of animals 8 days after treatment with anti-PD-1 antibodies or left untreated. (E) Statistical Scaffold map showing differences in immune cell proliferation (Ki67 expression) in the tumor microenvironment of animals 8 days after treatment with anti-PD-1 antibodies or left untreated.

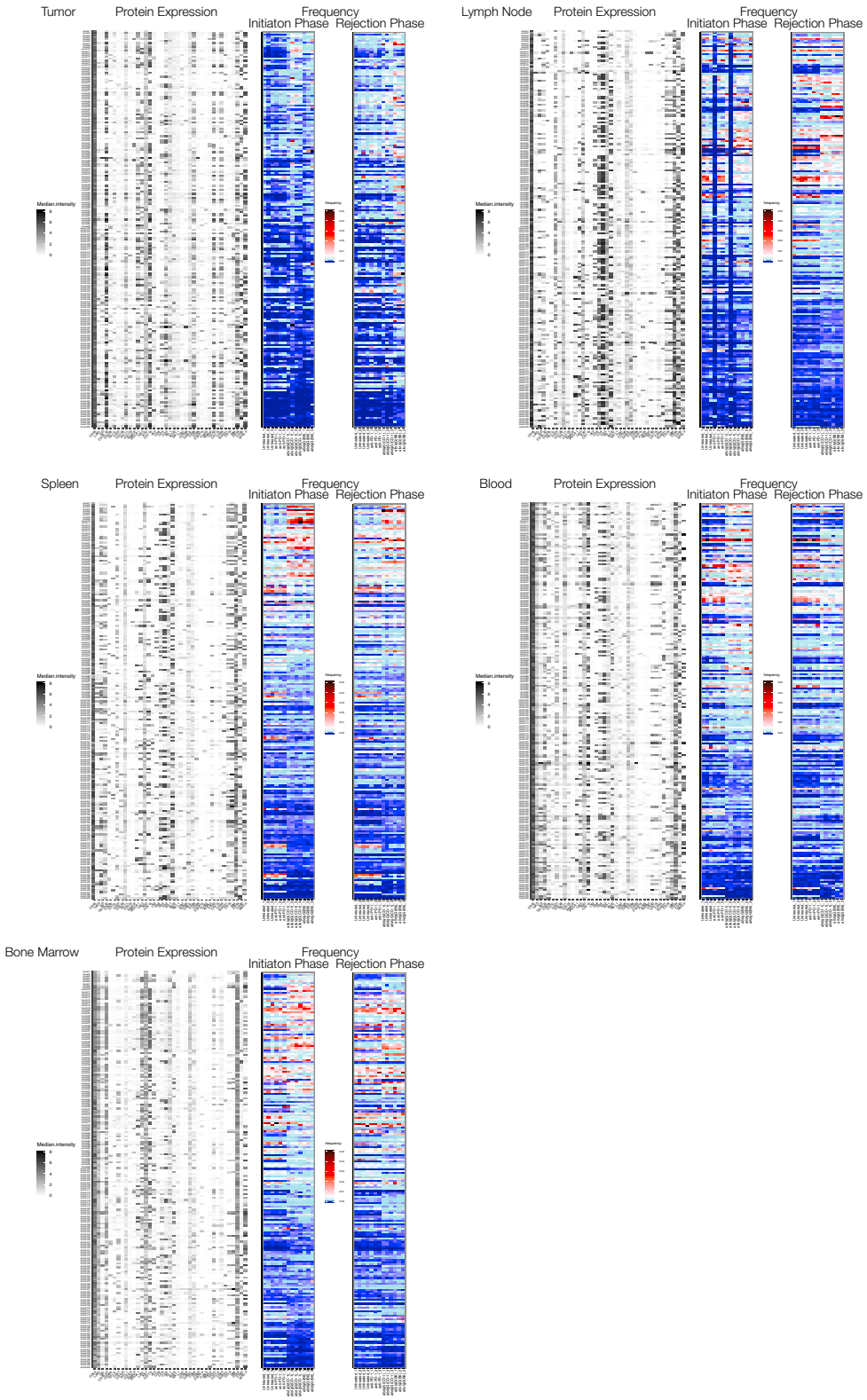

Figure S3. Immune Cell Cluster Frequencies and Protein Expression Profiles, Related to Figure 2

Heatmaps on the left (black and white) convey the protein expression profile or each immune cell cluster. Heatmaps on the right (colored) convey the frequency of each immune cell cluster in each animal at both time points.

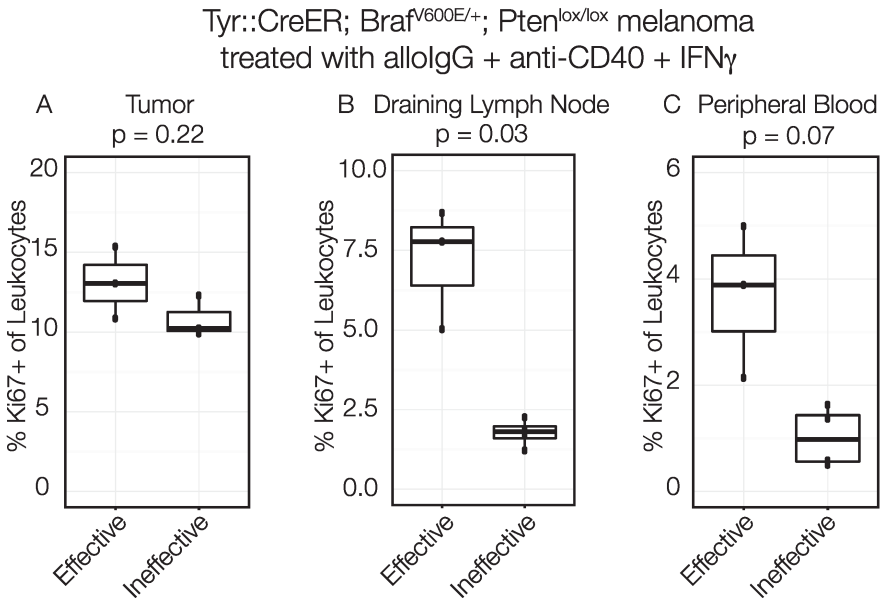

Figure S4. Sustained Immune Cell Proliferation in the Periphery after Effective Therapy Is Observed in BP Melanoma Mice as Well, Related to Figures 2, 3, and 4

(A–C) BP melanoma mice were treated with intra-tumoral injections of alloIgG antibodies (purified from the sera of CD-1 mice), anti-CD40 and IFNγ or were left untreated. Percent of leukocytes proliferating during the rejection phase (8 days after initiation of therapy) at various sites. (A) Tumor microenvironment. (B) Draining lymph node. (C) Peripheral blood. All p values reflect two-tailed, heteroskedastic t tests performed in R.

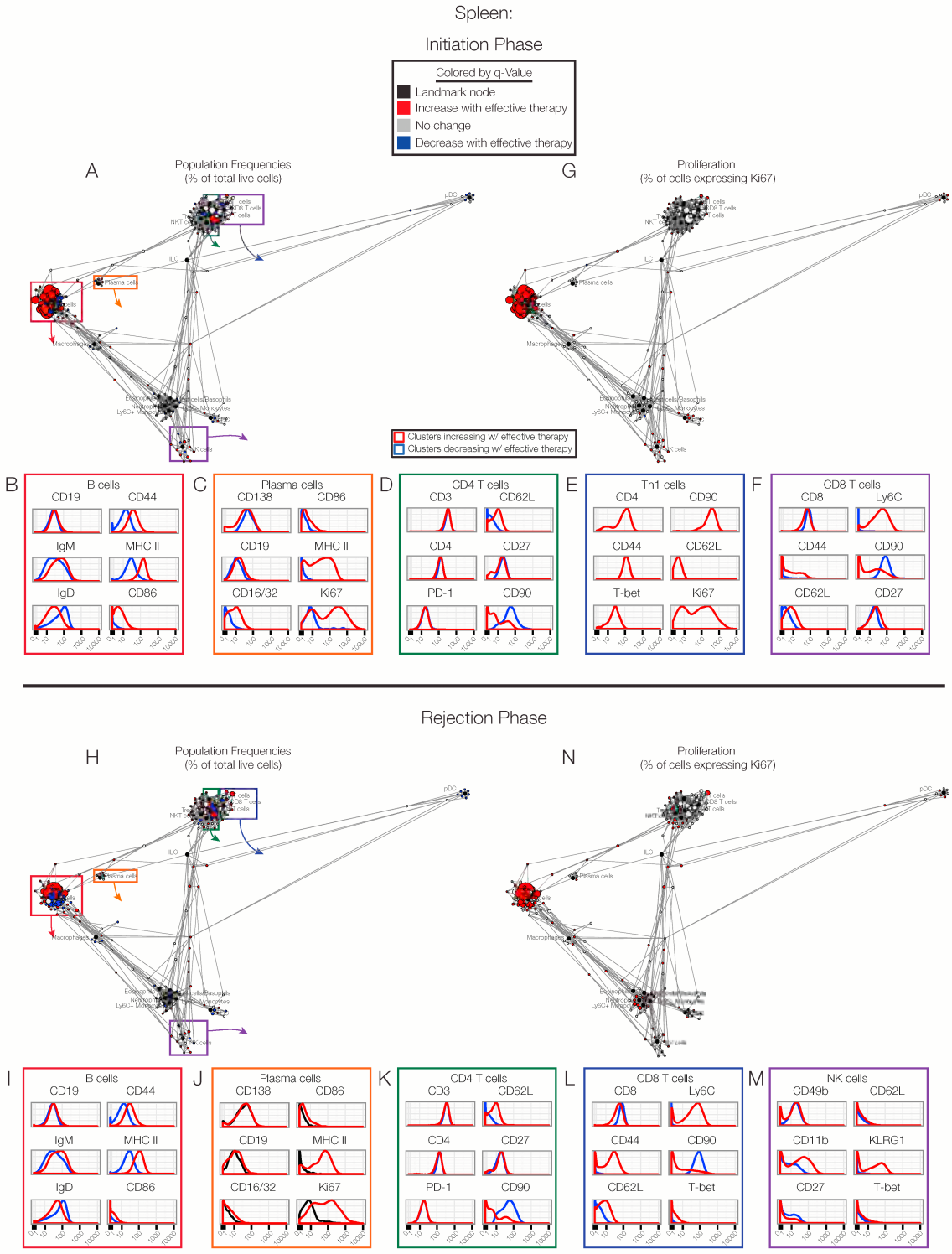

Figure S5. Immune Activation in the Spleen during Anti-tumor Immune Responses, Related to Figure 3

(A) Statistical Scaffold map of the spleen 3 days after the initiation of therapy. (B-F) Expression profile of cell clusters expanding with effective therapy (red histogram) versus those decreasing (blue histogram) on day 3 after initiation of therapy. (B) B cells. (C) Plasma cells. (D) CD4 T cells. (E) CD8 T cells. (F) NK cells. (G) Statistical Scaffold map of Ki67 expression in immune cell clusters in the spleen on day 3 after therapy. (H) Statistical Scaffold map of the spleen 8 days after the initiation of therapy. (I-M) Expression profile of cell clusters expanding with effective therapy (red histogram) versus those decreasing (blue histogram). (I) B cells. (J) Plasma cells. (K) CD4 T cells. (L) CD8 T cells. (M) NK cells. (N) Statistical Scaffold map of Ki67 expression in immune cell clusters in the spleen on day 8 after therapy.

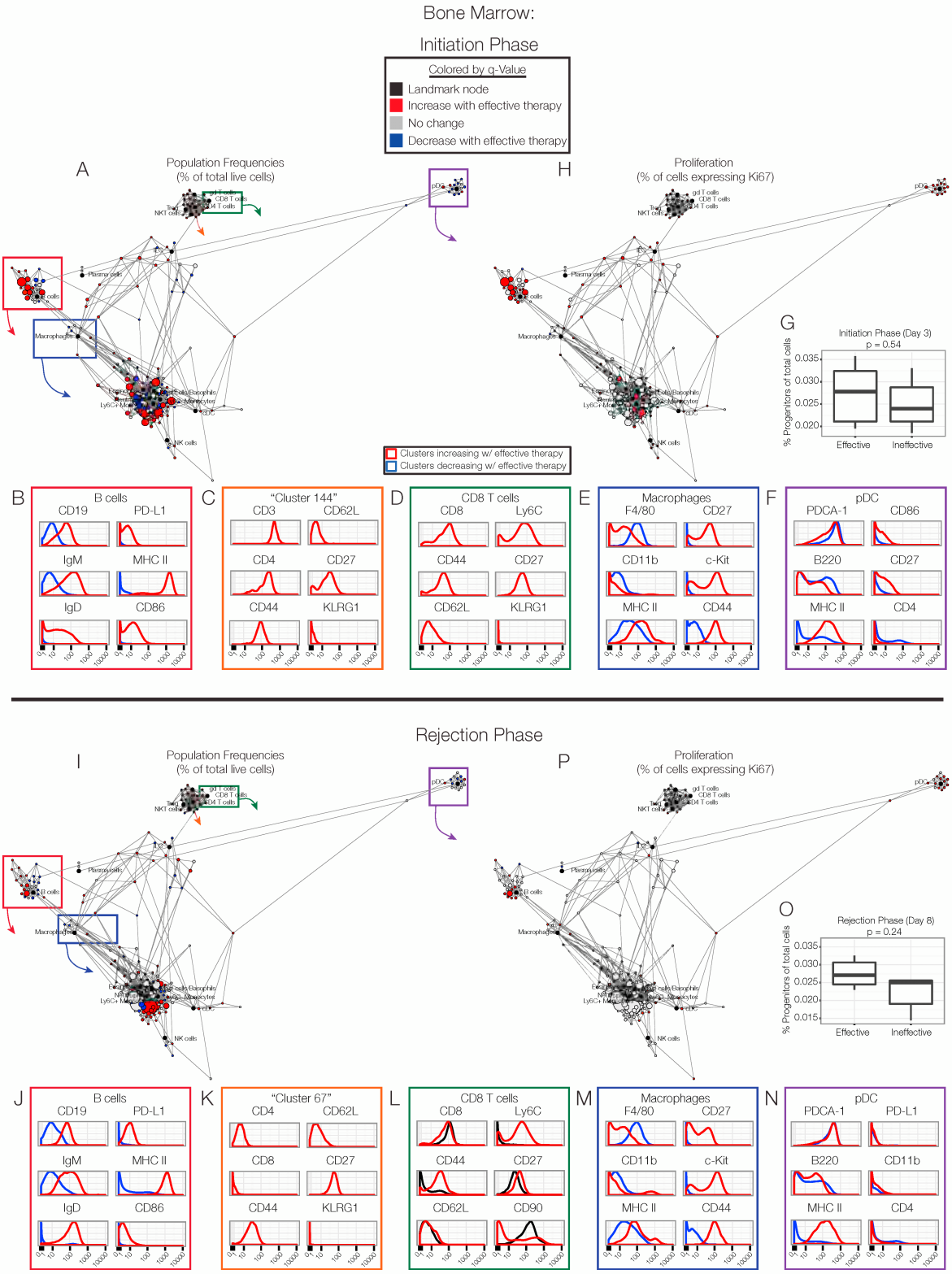

Figure S6. Anti-tumor Immune Responses Involve Widespread Activation in the Bone Marrow as Well, Related to Figure 4

(A) Statistical Scaffold map of the bone marrow 3 days after the initiation of therapy. (B) Expression profile of B cell clusters expanding with effective therapy (red histogram) versus those decreasing (blue histogram). (C) Expression profile of CD4 T cell cluster increasing with effective therapy. (D) Expression profile of CD8 T cell clusters increasing with effective therapy. (E) Expression profile of macrophage clusters expanding with effective therapy (red histogram) versus those

(legend continued on next page)

decreasing (blue histogram). (F) Expression profile of pDC clusters expanding with effective therapy (red histogram) versus those decreasing (blue histogram). (G) Frequency of hematopoietic progenitor cells (Lineage- cKit+) during the initiation phase. (H) Statistical Scaffold map of Ki67 expression in immune cell clusters in the bone marrow on day 3 after therapy. (I) Statistical Scaffold map of the bone marrow 8 days after the initiation of therapy. (J) Expression profile of B cell clusters expanding with effective therapy (red histogram) versus those decreasing (blue histogram). (K) Expression profile of CD4 T cell cluster increasing with effective therapy. (L) Expression profile of CD8 T cell clusters increasing with effective therapy. (M) Expression profile of macrophage clusters expanding with effective therapy (red histogram) versus those decreasing (blue histogram). (N) Expression profile of pDC clusters expanding with effective therapy (red histogram) versus those decreasing (blue histogram). (O) Frequency of hematopoietic progenitor cells (Lineage- cKit+) during the rejection phase. (P) Statistical Scaffold map of Ki67 expression in immune cell clusters in the bone marrow on day 8 after therapy. All p values reflect two-tailed, heteroskedastic t tests performed in R.

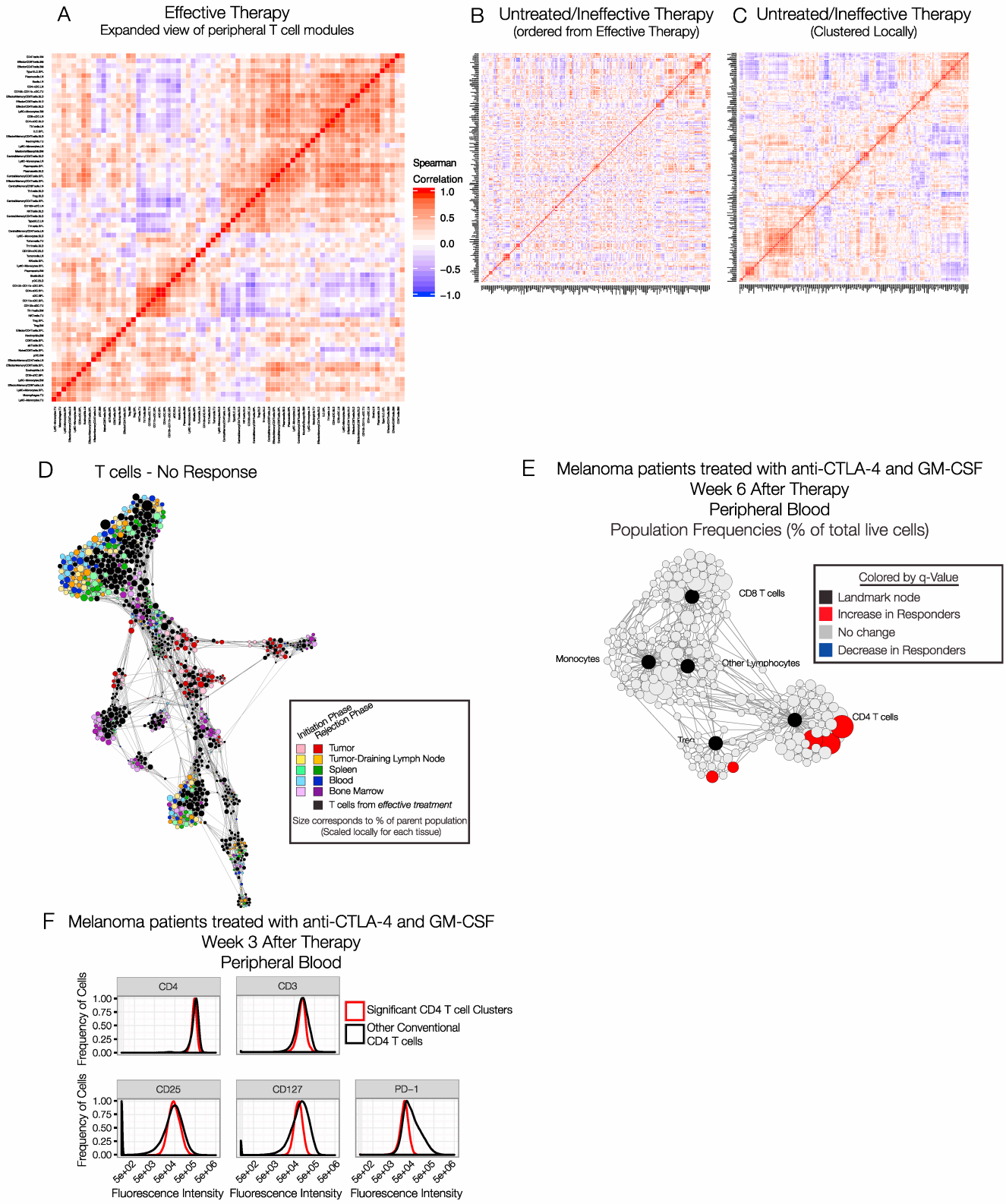

Figure S7. A CD4 T Cell Subset from the Periphery Is Sufficient to Mediate Anti-tumor Immunity, Related to Figure 6

(A) Zoomed in view of modules containing effector/memory T cell subsets in the peripheral sites. (B) Pairwise correlations of animals left untreated or treated with ineffective therapy. Order is imposed from the hierarchical clustering of the animals receiving effective therapy. (C) Pairwise correlations as in (B) but with

(legend continued on next page)

hierarchical clustering performed on the correlation coefficients from animals left untreated or treated with ineffective therapy. (D) T cell landscape as in Figure 6D, but with T cell subsets from mice receiving effective therapy in black and those subsets from untreated mice or those receiving ineffective therapy in colors reflecting their tissue and time point of origin. (E) Statistical Scaffold map highlighting differences in peripheral blood immune cell frequencies between responding and non-responding melanoma patients 6 weeks after anti-CTLA-4 and GM-CSF immunotherapy. (F) Histograms comparing the protein expression profiles of those CD4 T cell clusters that were significantly different in frequency between responders and non-responders at week 3 and the remainder of the CD4 T cell subsets that were not significantly different in frequency between these patient populations.